Accepted Manuscript in *Sensors and Actuators B: Chemical*

Published citation and link:
Khan, F. Z.; Abrego Tello, M.A.; Parette, D. N.; Fritsch, I.* "Sustaining Redox-Magnetohydrodynamics (R-MHD) Microfluidics by Switching Oppositely-Polarized Permanent Magnets: Synchronized Activation and Automation", *Sensors & Actuators B: Chemical*, **2021**, 346, 130415. (12 pages). DOI: https://doi.org/10.1016/j.snb.2021.130415

Supplementary Information link:
https://www.sciencedirect.com/science/article/pii/S0925400521009837?via%3Dihub#sec0105

Sustaining Redox-Magnetohydrodynamics (R-MHD) Microfluidics by Switching Oppositely-Polarized Permanent Magnets: Synchronized Activation and Automation

Foysal Z. Khan (mzkhan@uark.edu), Department of Chemistry and Biochemistry, University of Arkansas, Fayetteville

Miguel Abrego Tello (maabrego@uark.edu), Department of Chemistry and Biochemistry, University of Arkansas, Fayetteville

David N. Parette (dparette@uark.edu), Department of Chemistry and Biochemistry, University of Arkansas, Fayetteville

Ingrid Fritsch*(ifritsch@uark.edu), Department of Chemistry and Biochemistry, University of Arkansas, Fayetteville

06/11/2021

Abstract

A transformative advance in redox-magnetohydrodynamics (R-MHD) microfluidics is demonstrated that indefinitely extends its pumping duration with a miniaturizable approach, while preserving its uniqueness as an internal, self-contained, on-device, active and versatile pump that can also propel fluid in a loop. R-MHD can address the need for fine-tuning microfluidics in micro total analysis systems (μTAS) for multiple functions in an automated fashion that conventional external pumps with channels and/or valves that determine direction cannot fulfill. In MHD, a body force produced by the cross product of ionic current between strategically-activated electrodes and magnetic flux from a permanent magnet or electromagnet drives the fluid. Conducting-polymer-modified electrodes (e.g. with poly(3,4-ethylenedioxythiophene), PEDOT), involve faradaic processes to convert electronic current in the external circuit to ionic current in solution, overcoming bubble generation and electrode corrosion that limited previous MHD microfluidic applications. PEDOT-R-MHD pumping operates with a wider variety of solution compositions and without redox additives. However, pumping stops after complete oxidation/reduction of redox sites in the PEDOT films. The new advance reverses current between PEDOT-modified electrodes to discharge/recharge the polymer while simultaneously swapping permanent magnets of opposite polarities to sustain a constant, unidirectional pumping speed interrupted with brief pauses and without inductive heating. Factors affecting fluid velocities are described, including positions across the magnet assembly, current magnitudes and synchrony with current reversal. A model system (microbeads in biologically-compatible phosphate-buffered saline) is used, which can be generalized more broadly to biological and environmental applications, where starting, stopping, and indefinitely sustaining pumping of a sample are important.

Keywords: microfluidics, magnetohydrodynamics, permanent magnets, poly(3,4-ethylenedioxythiophene, electrode chips

1. Introduction

Magnetohydrodynamics (MHD) offers an elegant means to control fluid flow in microfluidic devices. Given its emerging utility in the scientific community, microfluidics propelled by MHD has captured great interest for applications where other microfluidic pumps are ineffective or unsuitable. Compatible with a variety of solvents and solution compositions, MHD can start, stop, reverse, and redirect fluid flow in a self-contained way, without requiring valves and channel sidewalls. Fluid flow can be tuned, stirred, and pumped in a loop on a scale of micrometers to centimeters. Automation and multiple functionalities are accomplished by programming the activation of strategically placed electrode features on MHD microfluidic devices without further redesign and reconstruction.

The uniqueness of MHD microfluidics has been exploited by several potentially high-impact applications (described below). However, MHD performance had been limited because of restrictions when operating in low-conducting solutions. Here, we implement modifications to the MHD microfluidics system that overcome those limitations and extend its pumping indefinitely. These innovations reposition MHD microfluidics for applications where its novel capabilities can now be harnessed. The new advance also enhances its performance in ways that were not previously possible.

MHD involves a body force, $\mathbf{F_B}$, that propels the solution. It is represented by the right-hand rule, $\mathbf{F_B} = \mathbf{j} \times \mathbf{B}$ (the magnetic portion of the Lorentz force), where the ionic current ($\mathbf{j}$, C/s m^2) passing through the solution and the magnetic flux ($\mathbf{B}$, T) are perpendicular to each other. The presence of both components generates a force on the ions in the third direction, orthogonal to both $\mathbf{j}$ and $\mathbf{B}$. Momentum transfers to the surrounding solution and causes the localized fluid to move

in the same direction as $\mathbf{F}_B$. The fluid is also subject to viscous forces that influence the fluid's net velocity and flow profile.

The principles and requirements to implement the forces induced by magnetic fields to achieve fluid motion for analytical chemistry applications have been reviewed by Weston et al. [1]. The ionic current, which is necessary for MHD, can be produced by applying an electronic current or a sufficiently large potential between two or more electrodes placed in the solution within the device. The solution must comprise of ions and solvents with sufficient dielectric constants compatible with electrochemistry, which spans a wide range (e.g. from water, 80.1 at 20 °C, to tetrahydrofuran, 7.52 at 22 °C) [2]. The magnetic field can be achieved with either a nearby permanent magnet or an electromagnet. Lastly, the position, orientation, and activation of electrodes and magnets are crucial in the tuning of MHD microfluidics.

Early applications of dc-MHD suffered from bubble formation (due to electrolysis of water) [3] and Joule heating [4] [5], adversely affecting fluid flow, which were later resolved by adding redox species to the solution to support the electron transfer (faradaic) processes at the electrodes. One electrode (the anode) oxidizes a redox species (e.g. ferrocyanide [6-12], iron(II) [6], hexaammineruthenium(II) [13, 14]) and the other electrode (the cathode) reduces a redox species (e.g. ferricyanide [6-12], iron(III) [6], hexaammineruthenium(III) [13, 14], Cu(II) [15], nitrobenzene [6]), resulting in ion compensation and migration from the surrounding solution that balance the charge and complete the circuit. Thus, the electronic current in the external circuit converts to ionic current in solution between the electrodes. dc-MHD microfluidics that uses redox species (dc-R-MHD) has demonstrated unique capabilities of interest for use in lab-on-chip applications [10]. Some notable features are mixing [15], stirring [11], and uniform and parallel flow profiles [8, 16]. When paramagnetic redox species are present, flow profiles can be further

manipulated through use of the additional magnetic field gradient force, $\mathbf{F}_{\nabla \mathbf{B}}$ [12]. dc-R-MHD microfluidics has been shown to function under immunoassay conditions [14] and with a spatially-defined electrochemical detector located downstream [13]. Possible interferences through chemical reactions with the redox species are possible; thus, careful selection of pumping species is essential. Also, electrochemically-driven, density-gradient convection can be substantial for high concentrations of redox species in solution and can contribute to the overall fluid motion [17, 18].

ac-MHD microfluidics without added redox species initially promised to minimize the bubble formation [19, 20] because a larger fraction of the current can come from charging of the electrode/solution double-layer rather than faradaic processes. A sinusoidally varying current required synchronization with a sinusoidally varying magnetic field from an electromagnet, thus complicating the setup and resulting in lower magnetic fields. Also, the frequency was too slow for the current to be solely sustained by double-layer charging. Thus, large voltage amplitudes were still needed to achieve high enough currents to pump at a practical speed, producing bubbles from faradaic processes of water electrolysis, and high frequencies produced inductive heating. Some ac-MHD applications include amplification of DNA with a polymerase chain reaction [21] and chemical separations by circular chromatography [22].

More recently, electrodes modified with the conducting polymer poly(3,4-ethylenedioxythiophene) (PEDOT) have been used for dc-R-MHD microfluidics to support faradaic current, eliminating the need to add redox species to the solution. Monomer units within the polymer backbone undergo oxidation and re-reduction at the PEDOT-modified anode and cathode, respectively, and can distribute the charge throughout the polymer chain due to its high conductivity. An ion current in solution between the two PEDOT-modified electrodes results from

charge compensation and migration. The electrochemical response of PEDOT-modified electrodes is similar to double layer charging, but exhibits an area-normalized capacitance that can be several orders of magnitude higher than a bare electrode. Like the redox pumping solutions, PEDOT-modified electrodes avoid bubble production and prevent electrode corrosion. However, unlike redox pumping solutions, use of PEDOT-modified electrodes allows R-MHD microfluidics to function in essentially any electrolyte solution and buffer that is compatible with biological samples and existing analyte detection schemes. Also, because the faradaic processes occur inside the polymer, density gradients are avoided while preserving the novel capabilities of MHD microfluidics [23, 24]. In addition, accumulation of paramagnetic analytes in high magnetic field gradients is possible without the influence of high concentrations of paramagnetic redox pumping species. A particularly important advantage is that the higher concentration of PEDOT redox sites immediately available at the electrodes allows higher currents, and therefore, faster fluid speeds than in past studies where redox species were added to the solution. However, there is a new limitation—the charge stored in PEDOT is quickly drained, especially at high currents, terminating fluid flow in a few seconds. Optimizing the quantity of PEDOT on electrodes prolongs duration of PEDOT dc-R-MHD pumping to a few minutes [25]. An image cytometry application demonstrates the substantial benefits of microfluidics pumped by PEDOT dc-R-MHD using a permanent NdFeB magnet [26]. When the PEDOT was fully discharged, the current at the electrodes was reversed, which also reversed the flow, so the cells could be counted or imaged again until the PEDOT charged up. These steps were repeated, extending the duration of PEDOT-MHD pumping indefinitely, which was possible using sinusoidal ac-MHD at a low frequency (10 Hz) to recharge the polymer [23]. Yet, the added current source for the electromagnet, synchronized instrumentation, and power requirements do not make this ac-MHD approach easy

to downsize. Also, the disadvantages of the low magnetic flux density from a sinusoidally varying electromagnet, timing complexity, and some inductive heating remains.

This paper introduces a transformative and automated approach to sustain dc-R-MHD pumping indefinitely without the challenges of ac-MHD while resolving other limitations that have restricted dc-MHD's use for microfluidics applications. The method as schematically depicted in Figure 1, charges and discharges PEDOT-modified electrodes by reversing the bias of the current with an interrupted square wave (ISW) function while simultaneously swapping permanent magnets with oppositely oriented fields by sliding them back and forth under the device. The applied current is provided by a battery-operated, handheld galvanostat that triggers actuation of the magnet switching assembly through a small controller board. The ISW current maintains a constant fluid speed, interjected with short pauses. Switching permanent magnets instead of sinusoidally varying an electromagnet eliminates inductive heating, harnesses higher magnetic flux densities, and greatly simplifies miniaturization. To demonstrate the concept, biologically-compatible phosphate-buffered saline (PBS) solution containing microspheres is used as a model for cells and to track fluid speed. The effect on fluid velocity of the position of the electrode-chip/fluid chamber device across an assembly of magnets oriented with polarizations opposite to each other is also evaluated.

2. Experimental

2.1. Chemicals and materials

Four nickel-coated, grade N40, NdFeB permanent magnets were acquired from Amazing Magnets, Irvine, CA. The two used for the manual magnet switching assembly were 0.14 T, 25.4

mm in diameter, and 3.17 mm in height. The two used for the automated magnet assembly were 0.37 T, 3.5 cm in diameter, and 1.27 cm in height. Sources and specifications of all other chemicals and materials are provided in Supporting Information Section S1.1.

2.2. Electrode chip design and fabrication

Two coplanar, individually-addressable, parallel band gold electrodes (1.5 cm long, 650 μm wide, and ~250 nm thick, separated by a 0.3 cm gap) were modified with PEDOT and used for the MHD pumping studies herein Supporting Information Section S1.2 includes details of the fabrication of the electrode chip and images of the electrode design with dimensions (Figure S-1).

2.3. PEDOT electrodeposition and characterization

All PEDOT electrodeposition and characterization studies were performed using a CH Instruments 760B potentiostat/galvanostat (Austin, Texas). Twelve consecutive cyclic voltammetry (CV) excursions were carried out on the chip electrodes at 0.005 V/s from -0.455 to 1.4 V vs Ag/AgCl (saturated KCl) reference electrode and using a Pt foil counter electrode in a propylene carbonate (PC) solution of 0.010 M EDOT monomer and 0.100 M $TBAPF_6$ electrolyte. Details of electrode preparation, polymer appearance (Figure S-1), polymer stabilization, and electrochemical characterization (Figure S-2–CV, chronoamperometry (CA), and chronopoteniometry (CP)) can be found in the Supporting Information Section S1.3.

2.4. Preparation of the R-MHD microfluidic chamber

The R-MHD microfluidic chamber was prepared by first inserting the PEDOT modified chip in a 20-pin edge connector (Sullins connector solutions, California) and ensuring proper alignment of the chip's pads with edge connector contacts. A PDMS gasket of ~762 μm thickness (measured dry), 3 × 2.5 cm in outer dimension, and with a cut-out opening of 2 × 1.8 cm, was placed on the chip to define the microfluidic chamber dimensions. An aliquot of 400 μL PBS: glycerol electrolyte and 12 μL of 10 μm polystyrene beads (Alfa Aesar, Massachusetts, USA) were added to the chamber and a glass cover-slip (2.4 × 3.0 cm and 0.16 mm thickness) was placed on top to serve as a lid. This solution composition will be denoted as the "buffer / glycerol / bead" solution throughout this paper. Two adjacent polymer-modified electrodes (Figure 2 (a) and (b)) were selected as working (electrode 1) and combined counter/quasi-reference electrode (electrode 2). Leads from the galvanostat (PalmSens 4 (PS4), Houten, The Netherlands) were clipped to the wires coming from the edge connector to individually control the two selected electrodes.

2.5. Manual magnet switching for proof-of-concept of sustained R-MHD fluid flow

Before automating the process, the magnets were switched manually to establish a proof of concept and to assess the effect of different magnet positions on R-MHD. Supporting Information Section S1.4 details the manual magnet switching apparatus (Figure S-3), its position on the microscope stage, and how R-MHD pumping was performed with this assembly.

2.6. Magnetic flux densities and the resulting horizontal fluid flow at different positions across the manual magnet switching apparatus.

Horizontal fluid velocities from R-MHD in the microfluidic chamber were analyzed for seven different positions over and between Magnets A and B of the manual magnet switching apparatus. A constant current of +50 (cathodic) and then – 50 μA (anodic) (non-IUPAC convention) were applied using the CH Instrument potentiostat/galvanostat for 20 s at a given position, but the fluid velocity only recorded during the cathodic step. The opposite bias of current was necessary to recharge the polymer film. The procedure was repeated for each subsequent position. The measurement window between the active electrodes in the chamber was made at a ~ 3 mm offset from a line connecting the centers of the magnets. For each magnet, the center measurement position (position b, for Magnet A and position f, for Magnet B) was aligned with its central axis (but with the 3 mm offset as described above). Two other positions were at the magnet edges (positions a and c for Magnet A and positions e and g for Magnet B), spaced out by ~ 1 cm from each magnet's center axis. Position d, was in-between and equidistant from the two magnets.

A dc magnetometer from Alpha Lab Inc., Utah, was used to measure the dc magnetic flux density at these positions with 0.01 gauss resolution (in the absence of the stainless steel plate). A more detailed magnetic flux density analysis was performed using numerical approximations with the COMSOL Multiphysics® platform, version 5.5 coupled with the AC/DC Module add-on. The specifics of the numerical approximations are included in Supporting Information Section S1.6. A comparison of the magnetic flux densities obtained from the numerical approximations to the experimentally measured values are included in Table S-1 (Supporting Information).

2.7 Automated magnet switching for sustained R-MHD fluid flow.

Figure 4 shows schematics of the magnet switching assembly and its interface to a servo board and the role of the galvanostat (current controller). A photograph and dimensions are provided in Figure S-5 of the Supporting Information.

2.7.1. The automated magnet switching assembly. The servo-driven magnet switching assembly was machined from a paper reinforced phenolic sheet with a nominal thickness of 12.7 mm. Two identical sections were machined to approximately 38 × 300 mm and served as the outer, stationary portion of the mechanism. These stationary sections had 3 × 12.7 mm nylon splines recessed into stopped dados in their inward-facing surfaces. These dados were machined using standard high-speed steel tooling on a vertical mill. The nylon splines serve as rails on which the 50 × 300 mm center section moves, which has corresponding full-length dadoes. Two magnets, approximately 12.7 mm thick and 35 mm in diameter, were press-fit into slightly undersized holes bored through the center section and are approximately spaced 85 mm center to center. This distance was maintained between the holes to ensure safe installment of these strong magnets.

These bores were made with a small adjustable boring head on the same vertical milling machine that was used for the stopped and full-length dadoes on the other pieces. The entire assembly was mounted on an aluminum sheet to facilitate installation and removal from the associated microscope stage. The rectilinear motion of the center section housing the magnets was accomplished by two servos acting on two rigid vertical pins sliding in 35 mm slots machined into identical aluminum arms approximately 115 mm long. The aluminum servo arms were machined on the vertical mill with high-speed steel tooling.

2.7.2. Coupling the current controller with the automated magnet switching assembly. Coupling of the current controller with the magnet switching assembly was accomplished by attaching a servo trigger board's input to a digital output line of the controller. The servo trigger board is a simple pulse width modulation device that moves a servo between two positions when there is a state change on the input. There is a pull-up resistor on the input, which allows the signal from the digital line from the current controller to be treated as a normally open switch. The default bi-stable settings of the microcontroller on the board were used. The configuration trimmers for initial position (when the input is open) and second position (when the input is closed) were adjusted to center the magnets under the stationary chip. Rapid acceleration of the magnets induced excess jitter in the video capture. Therefore, the rates of movement between the two positions were adjusted by the controlling potentiometer to minimize unwanted movement in the assembly. The output from the board that drives the servos was electrically parallel and the servos acted in a mechanical push-pull arrangement.

2.7.3. Sustained R-MHD pumping with the automated-switching assembly and galvanostat-triggering. Both the current for the fluid pumping and the triggering of the magnet switching were controlled by the PS4 in galvanostat mode, using the following procedure. The R-MHD microfluidic chamber or "chip-gasket assembly" was placed on Magnet A (M_A) and pumping electrodes were connected with the PS4 leads. Fluid pumping involved applying an ISW current waveform with ± 50, ± 100, and ± 200 μA between the PEDOT-modified pumping electrodes with a cut-off potential range of -1.0 to +1.10 V. (The convention for MHD pumping using this instrument assigns anodic current as positive, IUPAC convention.) These potential values were set to avoid excursions into the low capacity region of the PEDOT and accidental over-oxidation,

respectively. Electrode 1 and 2 ((Figure 2(b)) of the chip were used as working and combined counter/ quasi-reference electrodes, respectively. The two servos on the stationary rail of the automated magnet switching assembly were triggered by the galvanostat's digital signal commands through the aid of the servo trigger board.

Using scripting functionality in the PS4, a sequence of six commands were performed automatically. The first command applied an anodic current (e.g. +50 μA, +100 μA, or +200 μA) for 10 s using the CP technique while the chip-gasket assembly stayed over Magnet A. The second command was a "wait" time for 1 s, effectively an open circuit. The third command sent a digital signal (signal 1) to a connected device, which was the servo trigger to move the magnets and place Magnet B (M_B) under the chip. The fourth command applied a negative (cathodic) current using the CP technique with the same amplitude (e.g. -50 μA, -100 μA, or -200 μA, respectively) for 10 s while the chip stayed on Magnet B. The fifth and sixth commands were the "wait" time for 1 s and a digital signal (signal 2) to trigger the servo to bring back Magnet A (M_A) under the chip, respectively. This sequence of six commands was repeated three times for each of the applied current values (± 50, ± 100, and ± 200 μA).

2.8. Evaluation of fluid velocity

Fluid velocities were obtained by recording the movement of microbeads (added to the microfluidic chamber) with a Sony handycam camera (30 fps, HDR-XR 500 V) attached to a light microscope (Leica DM 2500M)) and by analyzing their motion. Particle image velocimetry (PIV) software (Dynamic Studio, v. 3.00, Dantec Dynamics, Copenhagen, Denmark) was used for analyzing fluid flow at a height of 385 μm in the R-MHD chamber at seven different positions over the static manual magnet switching assembly. Fluid flow for automated magnet switching

studies at a height of 640 μm was analyzed by particle tracking software, Tracker® [27]. More information about processing videos of microbead motion can be found in Supporting Information Section S1.7.

3. Results and Discussion

3.1. Electrochemical behavior of PEDOT as an indicator of R-MHD performance

Thick PEDOT films were electrodeposited on each of the band electrodes to achieve a high charge capacity to maximize the pumping time before reversing the current and switching the magnetic field direction. Electrochemical characterization of the PEDOT films by CV, CA, and CP was performed in the aqueous PBS:glycerol solution and compared to PEDOT films in prior R-MHD studies. See Figure S-2 and details in Supporting Information Section S2.1.

The capacitance determined from CV was 82.84 ± 0.28 mF/cm^2. The capacitance value (coulombs/volt) is a predictor for how much charge can be extracted from the PEDOT-modified electrodes, and therefore how long they can pump for a given potential excursion, during R-MHD.

The maximum current density obtained from CA was 143 ± 5 mA/cm^2, which is proportional to and therefore an indicator of the fastest achievable fluid speed expected for R-MHD pumping. Although we did not test for upper fluid speeds for R-MHD here, similar R-MHD microfluidic chambers have demonstrated speeds as high as 840 μm/s for 800 μA [25].

The CP response provides information about the duration of fluid pumping at a given current (or speed). For an applied current of ±50 μA, the potential reached the preset potential cutoffs of -0.2 V to +0.6 V vs. Ag/AgCl (saturated KCl) in 134 ± 2 s. Thus, we expect unidirectional pumping by R-MHD to be sustainable for this time at this rate of discharge of the

PEDOT film at a single electrode when the voltage range is limited to $\Delta E = 0.8$ V. If longer pumping is desired in the same direction with minimal disruption of fluid flow, then either the potential cutoffs can be expanded or the reverse current must be applied simultaneously with reversal of the magnetic field direction. Higher currents produce proportionally higher fluid speeds, but discharge the PEDOT at proportionally higher rates, shortening the pumping duration time in a single direction before switching the current and the magnetic field directions. However, for the same amount of discharge (coulombs), R-MHD will pump a fluid element the same distance, regardless of the pumping speed. The mathematical relationship [26] between pumping time and the PEDOT capacitance and resistance is discussed further in the Supporting Information Section S2.1.

3.2 Effect of magnet position on horizontal flow velocities and development of a magnet switching protocol

Fluid velocities in the manual magnet switching assembly were assessed across a path over two magnets oriented with polarizations opposite to each other to establish a magnet-switching protocol. Figure 3 depicts the PIV-analyzed flow profiles at 385 µm above the floor of the microfluidic chamber and across a ~2400 µm wide region between the activated PEDOT-modified band electrodes in three positions ("b", "c", and "d") over the manual magnet switching assembly for a constant cathodic current of 50 µA. This viewing window covers 3/4th of the gap between the active electrodes. Figure 3(a) shows the chip placement on position "b" which is along the mid-axis of Magnet A. The velocity vectors are parallel to each other and to the surface of the chip in the x-direction, giving an average of 12 ± 2 µm/s in the viewing window. The parallel flow pattern results from parallel ionic current paths in the y-direction across the gap between pumping

electrodes and a relatively uniform magnetic component B_z. Previous R-MHD studies have shown that the horizontal flow profile is uniform for a given height in a chamber between band electrodes and that the speed is at a maximum near the middle plane of the chamber and decreases toward the ceiling and floor [8, 16, 24, 26]. The speed at the top of the viewing window at position "b" in Figure 3(a) is smaller than that at the bottom, which can be explained by a PIV image that slices through more than one horizontal plane due to chamber tilt relative to the microscope's focal plane. In Figure S-6(c) of the Supporting Information, where the microfluidic chamber is at position "f", over the mid-axis of Magnet B, whose polarity is the opposite of Magnet A, the velocity vectors point in the opposite direction, ~~also~~ with evidence of chamber tilt. The average speed is -11 ± 2 μm/s, within error of that over Magnet A.

R-MHD fluid speeds are expected to scale proportionally with B_z [7]. Table S-1 in the Supporting information lists the magnetic flux densities measured with a magnetometer at the surface of the magnets and along the line connecting the magnet centers. Magnets A and B are similar, where the $|\mathbf{B_z}|$ values at their centers measure within 7% of each other, thus explaining the similar fluid speeds at positions b and f, respectively. In Figure 3(b) at the rightmost edge of Magnet A (position "c"), the velocity vectors are fastest in the left third (14 ± 1 μm/s) and slowest in the right third (4 ± 1 μm/s) of the viewing window. The trend follows an expected magnetic flux variation there. In addition, fluid flows mostly along the x-direction, but with a small y-component. A similar PIV image is obtained in position g, shown in Figure S-6(d) of the Supporting Information, except the fluid flows in the opposite direction because of the flipped magnetic field of Magnet B. It, too, has a slight angle to the flow direction. Likewise, mirror images of the velocity vectors at position c on Magnet A and position g on Magnet B are observed at positions "a" and "e", respectively (Figure S-6(a) and (b) of the Supporting information). This

mirroring behavior can be explained by the reversed distribution of the magnetic flux density on the opposite side of each of the magnets.

The fluid speed at the magnet's edge in position "c" is 1.2x that in position "b", which is lower than the ratio of the magnetometer values in those locations (1.7x). Our magnetic field measurements are unable to easily differentiate between contributions of the different components, B_x, B_y, and B_z with a high spatial resolution, which would be needed to explain the R-MHD fluid flow in these regions of large gradients and changing direction of the magnetic flux density.

In the region of position "d", where the magnetic flux density between the magnets is very low, one might expect an R-MHD force of zero. The measured fluid flow in this region, shown in Figure 3(c), is extremely slow (maximum ~ 1 μm/s), but is not zero, and has a direction parallel to the majority of the ionic current between the electrodes, j_y. Here, like at the edges of the magnets, the direction of the flow is not easily explained by MHD without more information about $|\mathbf{B}|$, B_x, B_y, and B_z. It cannot be explained by natural convection caused by illumination with the microscope, which would radiate inward or outward as the fluid rises in the center and falls at a larger radius.

Numerical approximations using COMSOL Multiphysics were performed to obtain more detailed maps of magnetic flux density over the manual magnet switching assembly. The simulations were first validated by comparing to measurements made by a magnetometer at the edges and center along the surface of each magnet, along a line containing the origins of both magnets. Table S-1 in the Supporting Information shows the averages for both, where standard deviations are reported for five separate measurements with the magnetometer and the variation of simulated values within the volume occupied by the magnetometer sensor. Figure S-7 shows the values from the numerical approximations in graphical form. The magnitude ($|\mathbf{B}|$) of the

simulated magnetic flux density at the centers of the two magnets (146 ±1 mT) is half that at the edges (294 ± 13 mT). The relative percent errors between the numerical approximations and the experimentally measured values for B_z are 3% and -4% at the center of Magnets A and B, respectively, and validate the simulations for these positions. The increased percent errors at the edges of the magnets, ranging from 8 to 24%, can be explained by sharp edges for the magnet geometry in COMSOL, whereas rounded edges were observed on the actual magnets and magnetometer measurements were less precise there. Thus, the map of simulated magnetic flux densities is most accurate near the centers, and caution should be taken when interpreting them directly on the edges. The simulations also confirm that B_z is the largest component, at least a factor of 0.87 of the magnitude of the magnetic field at all six of these positions, with its contribution being a factor of 1 of $|\mathbf{B}|$ at the centers. B_y has no contribution at the magnet centers and B_x contributes only a fraction of 0.009 and 0.02 at the centers and edges of the magnets, respectively.

Numerical approximations for $|\mathbf{B}|$, B_x, B_y, and B_z were then obtained at an offset of 3000 μm (in the +x direction) from a line connecting the magnet centers and at a constant height across the entire manual magnet switching assembly. This location is the same as where the videos of microbead motion were recorded to make Figures 4 and S-6. The height is 385 μm above the floor of the R-MHD or 2533 μm above the surface of the magnets, which accounts for the 1500 μm gap between magnet surface and bottom of electrode chip and the 648 μm electrode chip thickness. Figure S-8 of the Supporting Information plots the results across the entire assembly. The B_z component still dominates the magnetic field over most of the magnets and is zero between them. However, because of the 3000 μm offset in x, B_y and B_x play larger roles, especially at the magnet edges. In fact, $|B_z|$ becomes a maximum from 132 mT at the midline to 143 mT, going toward the

magnet's edge, but then drops to almost zero as $|B_y|$ substantially dominates with a maximum of 139 mT. However, it is reasonable to assume that B_y does not influence the R-MHD flow because the cross product with the ionic current density, **j**, which is dominated by j_y between the pumping electrodes, is zero. However, the j_z component associated with a curved electric field at the electrode, combined with the significant $B_{x\text{-}y}$ near the magnet's edge will contribute to the angled direction shown in Figure 3(b). Also, B_y is -14 mT halfway between the magnets, and that with a j_z component in ionic current could explain the small sideways fluid movement there due to $\mathbf{F_B}$, as well. B_x does not get larger than 35 mT near the edges and 14 mT at the midline of the magnets in this viewing region, and because of the short chamber height (762 μm), vertical fluid flow is unlikely from the cross product of j_y with B_x. At the ends of the electrodes, where j_x becomes important, the cross product with B_y will not be zero, but again, a vertical flow due to MHD is unlikely. We confine ourselves here to measurements between the parallel band electrodes. Consequently, B_z and the viscous forces will determine the speed and direction of the microfluidics between activated electrodes across the magnet assembly.

The fluid motion recorded in the viewing region shown in Figure 3 and S-6 results partially by $\mathbf{F_B}$ within that region as well as the influence of fluid motion due to $\mathbf{F_B}$ throughout the whole volume between pumping electrodes. Figure 5 provides maps of magnetic flux densities inside the *entire* pumping space, between outer edges of Electrodes 1 and 2 and along their entire length at a height of 385 μm above the floor of the chamber. (A schematic that illustrates the pumping region on the chip is provided in Figure S-9 of the Supporting Information.) In Figure 5(d) and (e), the magnitude of B_z is shown at positions a and c only in the region between the pumping electrodes where the video of fluid motion was recorded. In Figure 5(c), B_z is shown for the entire region between the pumping electrodes and at all seven positions. A comparison of B_z (Figure 5(c)) to

B_y (Figure 5(b)), shows the influence of B_y is much more extensive than that of B_z, because of its larger variation across that space.

The Supporting Information provides additional magnetic flux density maps. Figure S-10 shows similar variations in $|\mathbf{B}|$, B_x, B_y, and B_z in a horizontal plane at a height of 640 μm in the pumping volume between Electrodes 1 and 2 as for 385 μm (Figure 5), but at slightly lower magnetic flux densities. For example, at the center of Magnet A, B_z is 130 mT at a 385 μm height in the chamber and just 128 mT at 640 μm. Figure S-11 provides vertical slices across the breadth of the pumping volume, showing more completely the variation in magnetic flux densities from the floor to the ceiling of the chamber. These figures further confirm that the region with the least variation of magnetic flux densities along the length, height, and breadth of the pumping region is at the center of the magnets, positions "b", and "f." The averages and standard deviations over the entire pumping region at position "b" of $|\mathbf{B}|$, and the absolute values of B_x, B_y, and B_z are 138 ± 7, 21 ± 15, 6 ± 4, 135 ± 5 mT, respectively. The magnitude of B_z dominates the other components and only varies by 4%. The variation in B_x is much larger than the other components, because the ends of the 1.5 cm-long pumping region, which lies along the x-direction, are closer to the edges of the magnet where B_x is the strongest. Both B_x and B_y are not expected to contribute significantly to the MHD-driven flow pattern, because a vertical force from $F_{Bz} = j_y \times B_x$ is counteracted by viscous forces in the thin chamber and was not observed [9]. B_y is very small and the cross product $j_y \times B_y = 0$.

These microfluidics studies and assessment of magnetic flux densities across a magnet switching assembly reveal important considerations toward achieving predictable, unidirectional R-MHD pumping with a relatively constant speed and minimal perturbation. This knowledge was implemented in designing the magnet-switching protocols. An important point is that the magnet

does not need to larger than the device; it only needs to be larger than the pumping region on the device. One approach to sustain a constant fluid speed when the chamber moves over the magnet is to tune the current synchronously with the mapped B_z component. However, the edges of the magnet (positions a, c, e, and g, for example) would need to be avoided where steep changes in B_z could simultaneously induce different speeds between the pumping electrodes, like those in Figures 4(b) and S-6(a, b, d). A simpler approach was used here, instead, by first holding the device stationary over with the activated electrodes centered at the magnet. In this region, the B_z is the most uniform across the gap, along its length and through the height of the chamber. Second, the electrodes are inactivated, followed by swapping the underlying magnets. Once the center of the magnet with the reverse polarity is positioned beneath the microfluidic chamber, a reverse current is applied and pumping can continue in the same direction. This approach results in a repeated pump-pause cycle.

The proposed magnet switching approach was tested by manually swapping the magnets under the microfluidic chamber. This was performed with the manual magnet switching assembly shown in Figure S-3. A 50 μA current was chosen as a starting point, which we know can be applied for as long 134 s over a 0.8 V range (from -0.2 V to +0.6 V vs. Ag/AgCl (sat'd KCl) based on the CP study, although we limited the pumping times to 10 s. This current is also far below the maximum current in the CA response (~14 mA) and thus, PEDOT can support the current without overoxidation. The programmed ISW function, the fluid displacement, and the fluid speed over 40 s involving three pumping periods for the manual magnet switching assembly are shown in Figure S-4 of the Supporting Information. The experiment involved applying a 50 μA step for 10 s, followed by a 5 s period where the electrodes were at open circuit (i = 0), applying current with opposite bias for 10 s, followed by another 5 s at open circuit, and then repeating this sequence.

The long time of 5 s at "open circuit" was set to accommodate the imprecise manual switching of the magnet of opposite-field direction (Magnet A or B). Switching was achieved by pushing or pulling the ruler to which the magnets were affixed under the chip assembly at the appropriate time while monitoring the chronopotentiometric response and listening for the audible indicator (see Section 2.5 and Section S1.4 of the Supporting Information). Therefore, the actual time swapping of magnets began and the time it took to complete the translation of magnets from position b to position f and back were slightly different for each cycle. The synchronized change in magnet and current bias sustained the body force ($\mathbf{F_B}$) direction and magnitude, and the fluid flows in a single direction at the same speed, but interrupted by pauses that are as short as the switching time. A more quantitative discussion is provided in Supporting Information Section S2.2.

3.3 Unidirectional fluid flow achieved by automated switching of magnets under the chip.

The automated magnet switching assembly (Figure 4 and Figure S-5 in the Supporting Information) was constructed with a similar linear design as the manual one, with the magnets placed on a stage that slides beneath the chip assembly. Phenolic sheet was used to accommodate the stronger (0.37 T measured at magnet center) and larger magnets (3.5 cm diameter and 1.27 cm high), which were press-fit into the stage, 5 cm apart. Nylon splines served as rails to facilitate sliding. The PS4 galvanostat triggered a controller board that slides the stage to swap the magnets with timing, acceleration and deceleration that minimizes jarring and overshooting.

Video S-1 in the Supporting Information shows the operation of the automated magnet switching assembly and unidirectional fluid flow, interspersed with short pauses, in the measurement region of the chip, where current between the PEDOT-modified electrodes is

synchronized with the exchange of the magnets. Similar to the manual magnet switching approach, the current was applied for 10 s, followed by an open circuit period, but of only 1 s instead of 5 s, after which a trigger is sent to the controller board to start translating the magnet stage. Then the oppositely biased current is applied for another 10 s with the chamber positioned over the other magnet, followed by 1 s open circuit and trigger steps. Also, the distance between magnets is 5 cm, instead of 2.5 cm (to minimize difficulty constructing the device with such strong magnets). Thus, to bring the new magnet beneath the chip assembly before the new current was applied, the translation speed of the automated apparatus was >5 cm/s, or 10+ times that of the manual one.

Three different currents ± 50, ± 100, and ± 200 μA applied between two PEDOT-modified electrodes were investigated to produce R-MHD fluid flow using the automated magnet switching assembly. Higher currents discharge PEDOT faster. However, the expected pumping duration of 33.5 s across a 0.8 V range at 200 μA, $1/4^{th}$ that for 50 μA, is sufficiently long to sustain a current for 10 s intervals in the switching protocol. Figure 6 compares the applied current waveforms, with the resulting fluid displacements and velocities for the first 22 s of video of a given experiment. As with the manual magnet switching study, the velocity is reproducibly achieved over each magnet. The fluid speed (50 ± 2 μm/s) is faster at 50 μA than in the manual switching studies by a factor of 2.7 ± 0.1, which is within one standard deviation of the proportionally higher magnetic flux density of 0.37 T (a factor of 2.6). The flow was measured in a horizontal plane 255 μm higher from the chamber floor than the manual switching studies, which will slow the speed slightly than that toward the middle of the chamber. Also, the changes in B_z across the pumping region and height at positions b and f are not expected to be substantial based on our magnet simulations (see Figure S-11(c) for vertical changes in B_z and compare Figure 5(c) with Figure S-10(c) for distributions of B_z across the pumping region at those two heights). Likewise, increases in the

applied current of 50 μA, 100 μA, and 200 μA increase the fluid speed proportionally of 50 ± 2 μm/s, 98 ± 2 μm/s, and 193 ± 7 μm/s, as expected. The predictable changes to fluid speed for these magnet switching apparatuses, based on a change in magnetic flux density and applied current and the reproducibly produced unidirectional flow over both magnets, reiterate the well-behaved and highly tunable nature of R-MHD microfluidics.

The noticeable rise time and fall time in fluid speed at the beginning and end when applying current over a 10 s period (Figure 6(c)) were not observed in the manual switching studies (Figure S-4(c)). We believe this to be a consequence both of the uncertainty in knowing the starting and stopping point in the video when the magnets were swapped as well as a shorter time increment between video frames. That increment time for the automated switching studies is about twice as much (0.67 s between points), leading to a lower resolution when fluid speed changes the most. We expect that data collection at a higher rate would produce sharper transitions in the plots of velocity.

Another difference in the automated switching studies of Figure 6(c) compared to the manual ones in Figure S-4(c) is that fluid speed never drops to zero when the electrodes are at open circuit. This could also be due to the low time resolution. In addition, the drop in fluid speed lasted longer than the 1 s that was set for "open circuit". This can be explained by the subsequent triggering step, which also takes time to execute. Based on Figure 6(b) and (c), it appears that these two steps take a total of about 2 s together. Tighter control over the timing of the trigger and duration of open circuit should lead to shorter pause times and a more reproducible fluid response there.

4. Conclusions

We have developed a galvanostat-triggered, automated magnet switching method, coupled with R-MHD with PEDOT-modified electrodes to generate semi-continuous, unidirectional microfluidics pumping for an unlimited time. Repetitive application of oppositely biased currents in synchrony with swapping permanent magnets of opposite field directions ensures regeneration of the conducting polymer's charge while the MHD force can continue to propel fluid at a constant high speed in the same direction, regardless of the polymer's capacity and, with brief pauses. This ISW approach can be largely described as dc-MHD, avoiding the inductive heating, sinusoidally varying speeds, and the more complex instrumentation associated with ac-MHD. The approach also preserves the unique tunability of R-MHD and its compatibility with fluids from organic solvents to those that are biologically compatible, demonstrated here. Microfluidics applications that were limited by previous implementations of dc-MHD and ac-MHD, can now be revisited, and expanded, especially for biochemical reactions and biological applications requiring liquids with a delicately balanced compositions, times longer than a few minutes to achieve higher throughput for analysis, and where unidirectional pumping is critical as for chemical separations.

Future modifications of the applied current waveform and control of the translational stage could further shorten the pause time between MHD flow conditions. One can be facilitated by improved control over triggering of the magnetic switching apparatus when the electrodes are at open circuit. Another possibility is to synchronize a programmed ionic current with the varying magnetic field while the microfluidic chamber travels across each magnet. This advance could utilize the entire path across the permanent magnets while sustaining a constant MHD force during a deceleration and acceleration period when reversing direction, allowing for a more continuous motion of the magnets. Lastly, avoiding vibrations associated with reversal of direction altogether

while improving switching time could be achieved by housing of multiple magnets of alternating fields on a circular base that continuously rotates in a single direction beneath the microfluidic chamber [28].

Author Contributions

The manuscript was written through contributions of all authors. All authors have given approval to the final version of the manuscript.

Appendix A. Supplementary Material

Supporting information includes additional chemicals and materials; details of electrode fabrication, PEDOT electrodeposition and electrochemical characterization, apparatus and R-MHD pumping with the manual magnet switching assembly, numerical approximations, and evaluation of fluid velocity; photographs of a chip before and after PEDOT deposition on electrodes; figures of PIV analysis of horizontal flow profiles, various graphical representations of numerical approximations of magnetic flux densities across the manual magnet switching assembly, and the automated magnet switching assembly; a table of comparisons of measured and simulated magnetic flux densities at magnet surfaces; and a video of automated magnet switching and resulting R-MHD fluid flow.

Declaration of Competing Interest

I. Fritsch, F. Z. Khan and D. N. Parette declare a potential conflict of interest as they are listed as inventors on a patent filed by the Board of Trustees of the University of Arkansas concerning MHD technologies and methods. The other author declares no conflict of interest.

Acknowledgments

We are grateful for financial support from the National Science Foundation (CMI-1808286) and the Arkansas Bioscience Institute, the major research component of the Arkansas Tobacco Settlement Proceeds Act of 2000. We thank Mr. Mathew Gerner for the initial chip design and Mr. Benjamin J. Jones for design modifications.

References

[1] M.C. Weston, M.D. Gerner, I. Fritsch, Magnetic Fields for Fluid Motion, Anal Chem, 82(2010) 3411-8.

[2] J. Rumble, CRC Handbook of Chemistry and Physics, 100th ed.: CRC Press; 2020.

[3] L. Wang, L. Flanagan, A.P. Lee, Side-Wall Vertical Electrodes for Lateral Field Microfluidic Applications, J Microelectromech Sys, 16(2007) 454-61.

[4] A. Homsy, V. Linder, F. Lucklum, N.F. de Rooij, Magnetohydrodynamic pumping in nuclear magnetic resonance environments, Sens Actuat B-Chem, 123(2007) 636-46.

[5] A. Homsy, S. Koster, J.C.T. Eijkel, A. van den Berg, F. Lucklum, E. Verpoorte, et al., A high current density DC magnetohydrodynamic (MHD) micropump, Lab Chip, 5(2005) 466-71.

[6] P.U. Arumugam, E.S. Fakunle, E.C. Anderson, S.R. Evans, K.G. King, Z.P. Aguilar, et al., Redox Magnetohydrodynamics in a Microfluidic Channel: Characterization and Pumping, J Electrochem Soc, (2006) E185-E94.

[7] M.C. Weston, I. Fritsch, Manipulating Fluid Flow on a Chip Through Controlled-Current Redox Magnetohydrodynamics, Sens Actuat B-Chem, 173(2012) 933-44.

[8] V. Sahore, I. Fritsch, Flat Flow Profiles Achieved with Microfluidics Generated by Redox-Magnetohydrodynamics, Anal Chem, 85(2013) 11809-16.

[9] F. Gao, A. Kreidermacher, I. Fritsch, C.D. Heyes, 3D Imaging of Flow Patterns in an Internally-Pumped Microfluidic Device: Redox Magnetohydrodynamics and Electrochemically-Generated Density Gradients, Anal Chem 85(2013) 4414−22.

[10] C. Das, G. Wang, F. Payne, Some practical applications of magnetohydrodynamic pumping, Sens Actuat A-Phys, 201(2013) 43-8.

[11] V. Sahore, I. Fritsch, Microfluidic rotational flow generated by redox-magnetohydrodynamics (MHD) under laminar conditions using concentric disk and ring microelectrodes, Microfluid Nanofluid, 18(2015) 159-66.

[12] V. Hähnel, F.Z. Khan, G. Mutschke, C. Cierpka, M. Uhlemann, I. Fritsch, Combining magnetic forces for contactless manipulation of fluids in microelectrode-microfluidic systems, Sci Rep, 9(2019) 5103.

[13] V. Sahore, I. Fritsch, Redox-Magnetohydrodynamics, Flat Flow Profile-Guided Enzyme Assay Detection: Toward Multiple, Parallel Analyses, Anal Chem, 86(2014) 9405-11.

[14] M.C. Weston, C.K. Nash, I. Fritsch, Redox-Magnetohydrodynamic Microfluidics Without Channels and Compatible with Electrochemical Detection Under Immunoassay Conditions, Anal Chem, 82(2010) 7068-72.

[15] S. Qian, H.H. Bau, Magneto-hydrodynamic stirrer for stationary and moving fluids, Sensor Actuat B-Chem, 106(2005) 859-70.

[16] E.C. Anderson, M.C. Weston, I. Fritsch, Investigations of Redox Magnetohydrodynamic Fluid Flow At Microelectrode Arrays Using Microbeads, Anal Chem, 82(2010) 2643-51.

[17] V. Sahore, A. Kreidermacher, F.Z. Khan, I. Fritsch, Visualization and Measurement of Natural Convection from Electrochemically-Generated Density Gradients at Concentric Microdisk and Ring Electrodes in a Microfluidic System, J Electrochem Soc, 163(2016) H3135-H44.

[18] K. Ngamchuea, S. Eloul, K. Tschulik, R.G. Compton, Advancing from rules of thumb: quantifying the effects of small density changes in mass transport to electrodes. Understanding natural convection, Anal Chem, (2015) DOI: 10.1021/acs.analchem.5b01293.

[19] A.V. Lemoff, A.P. Lee, An AC magnetohydrodynamic micropump, Sens Actuat B-Chem, 63(2000) 178-85.

[20] A.V. Lemoff, A.P. Lee, An AC Magnetohydrodynamic Microfluidic Switch for Micro Total Analysis Systems, Biomed Microdevices, 5(2003) 55-60.

[21] J. West, B. Karamata, B. Lillis, J.P. Gleeson, J. Alderman, J.K. Collins, et al., Application of magnetohydrodynamic actuation to continuous flow chemistry, Lab Chip, 2(2002) 224-30.

[22] J.C.T. Eijkel, C. Dalton, C.J. Hayden, J.P.H. Burt, A. Manz, A circular ac magnetohydrodynamic micropump for chromatographic applications, Sens Actuat B-Chem, 92(2003) 215-21.

[23] C.K. Nash, The 2014 Colin G. Fink Summer Research Fellowship — Summary Report: Advanced Microfluidic Pumping at Poly(3,4-ethylenedioxythiophene)-Modified Electrodes via AC-Magnetohydrodynamics, The Electrochemical Society Interface, 23(2014) 79-80.

[24] C.K. Nash, I. Fritsch, Poly(3,4-ethylenedioxythiophene)-Modified Electrodes for Microfluidics Pumping with Redox-Magnetohydrodynamics: Improving Compatibility for Broader Applications by Eliminating Addition of Redox Species to Solution, Anal Chem, 88(2016) 1601-9.

[25] F.Z. Khan, I. Fritsch, Chip-Scale Electrodeposition and Analysis of Poly(3,4-ethylenedioxythiophene) (PEDOT) Films for Enhanced and Sustained Microfluidics Using DC-Redox-Magnetohydrodynamics, J Electrochem Soc, 166(2019) H615-H27.

[26] F.Z. Khan, J.A. Hutcheson, C.J. Hunter, A.J. Powless, D. Benson, I. Fritsch, et al., Redox-Magnetohydrodynamically Controlled Fluid Flow with Poly(3,4-ethylenedioxythiophene) Coupled to an Epitaxial Light Sheet Confocal Microscope for Image Cytometry Applications, Anal Chem, 90(2018) 7862-70.

[27] D. Brown, Tracker: Video Analysis and Modeling Tool, 2020.

[28] I. Fritsch, F.Z. Khan, D. Parette, Magnetohydrodynamic Microfluidic Systems Including Modified Electrodes And Methods Of Using The Same, BOARD OF TRUSTEES OF THE UNIVERSITY OF ARKANSAS (Little Rock, AR, US), US, 2020.

Figure captions

Figure 1: The concept of magnet switching provides indefinitely sustained MHD microfluidics in one direction. Shown is a representative plot of fluid displacement and applied current as a function of time (an intermittent square wave, ISW) during a switching experiment. Top-down schematics are depicted for the relative positions of the chip and the two magnets with fields in opposite directions during the experiment at each time interval, with the resulting direction of fluid movement. In this particular depiction, a current of +i (anodic) is applied for a given duration while Magnet A (M_A) is under the chip, the circuit switches to open circuit for another period of time while Magnet B is moved under the chip, and a current of -i (cathodic) is applied for another duration while Magnet B (M_B) is under the chip. Coordinates indicate relative orientation of ionic current in the solution, **j**, magnetic flux density, **B**, and resulting MHD force, $\mathbf{F_B}$, at each experiment interval. The direction of magnetic field of Magnet A points out of page and that of Magnet B points into the page.

Figure 2: Experimental setup. In (a), the chip-gasket assembly is placed on the permanent magnet (Magnet A, 0.37 T, on the automated magnet switching assembly is shown here) that is housed on a translational stage. The whole chip-gasket-magnet assembly is located on the microscope stage. A glass coverslip is placed over the gasket which contains the "buffer / glycerol / beads" solution. The pair of electrodes labeled as "Modified Electrodes" are the ones that were activated for pumping fluid. The edge connector maintains individual electrical connection between electrode and current controller. The schematic in (b) depicts a chip and solution region defined by the opening in the PDMS gasket (outlined by yellow dashed lines) over a magnet with the direction

of fluid flow (blue arrows) between and around the activated electrodes for a given direction of ionic current (green arrow) and magnetic field direction (red bullet). Electrodes 1 and 2 served as the working and combined counter/reference electrodes, respectively.

Figure 3: Schematics and PIV analysis of fluid flow from the top view perspective of a chip placed over the manual magnet switching assembly at different positions using a translational stage. A constant 50 μA cathodic current was applied between Electrode 1 vs Electrode 2 and the video of microbead motion was obtained at a height of 385 μm above the floor of the fluid chamber. In (a), the measurement region of the chip was placed over position “b" (at the middle of magnet A. where field points upward), with a 3 mm offset from the magnet’s center) and the vectors obtained by PIV analysis in the expanded view show the characteristics of the experimental fluid velocities. (b) and (c) show figures as in (a) but for the chip placed over position “c", at the edge of Magnet A, and position “d", between the magnets, respectively. (Note that the white lines in the PIV images are insulated leads that connect to other electrodes on the chip and are used to confirm a consistent location for video recording. The small square in each schematic shows where these features and video recordings are located between the activated electrodes.)

Figure 4: The automated magnet switching system has four distinctive parts: the computer to run galvanostat software, galvanostat (current controller), servo trigger board and translational stage with magnets having opposing field directions, and chip-gasket assembly. The galvanostat is connected with the computer through USB C cable. The servo trigger board’s input is connected to a digital output line of the current controller through a 15-pin D-sub auxiliary connector. The

servo trigger board output lines connect with the servos S_A and S_B that attach to the stationary rail of the translational stage. The translational stage has one moving section (5 × 30 cm) that attaches through nylon splines to two identical stationary sections (3.8 × 30 cm), so that the translational section can move freely. Two NdFeB permanent magnets, oriented with opposite field directions, and 50 mm apart from magnet edge to edge, are press-fit into holes bored through the center section. (*Image of PalmSens4 used with permission from PalmSens. Image of controller board used with permission from SparkFun Electronics, Photographer Juan Peña.*)

Figure 5: Results from numerical approximations of the three components of magnetic flux density: (a) B_x, (b) B_y, and (c) B_z. Horizontal slices (xy planes) are shown through the space between outer edges of the activated band electrodes (4300 μm), along their length (1.5 cm) and at 385 μm from the floor of the chamber at seven different regions across the manual magnet switching assembly having dimensions as those shown in Figure S-5 of Supporting Information. In (d) and (e), expanded maps of component B_z over a 1945 μm x 1107 μm area for the given x and y locations are shown for the chip located at positions a and c over the left and right edge of Magnet A, respectively.

Figure 6: Results involving R-MHD microfluidics with the automated magnet switching assembly. (a) ISW current functions for ±50, ± 100, and ± 200 μA. (b) Fluid displacement (μm) resulting from the ± 50 μA applied current with the corresponding switched magnets. (c) Fluid velocities generated from ±50, ± 100, and ± 200 μA applied currents. The fluid velocities (at ±50 μA applied current) in (c) were derived from the fluid displacement data in (b). All data shown in

the figure were acquired from the first 22 s of the first cycle of a 5 cycle experiment, corresponding to 10 s of pumping at a constant anodic current over magnet A, a 2 s period at open circuit, and another 10 s of pumping at a constant cathodic current over magnet B. Velocities in (c) are from averaging the motion of 10 microbeads, and the error bars correspond to ± one standard deviation.

Figure 1

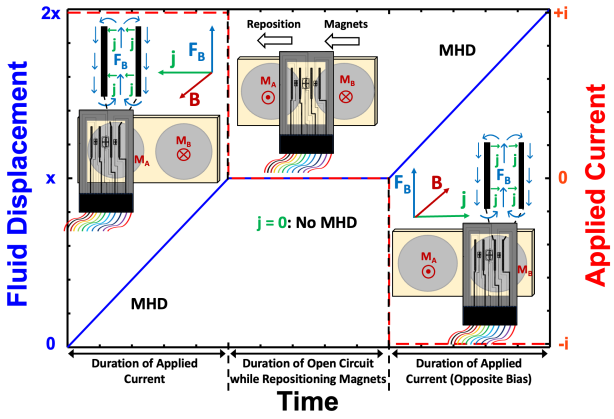
2x
x
0
Fluid Displacement
+i
0
-i
Applied Current
Reposition
Magnets
MHD
MHD
j = 0: No MHD
Duration of Applied Current
Duration of Open Circuit while Repositioning Magnets
Duration of Applied Current (Opposite Bias)
Time

Figure 2

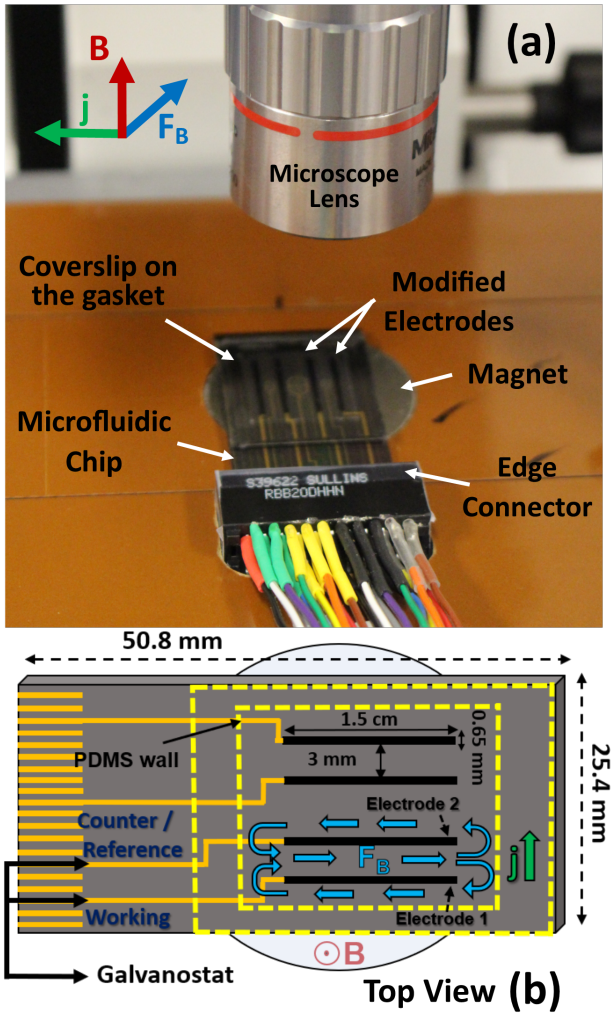
B
j
F_B
(a)
Microscope Lens
Coverslip on the gasket
Modified Electrodes
Magnet
Microfluidic Chip
Edge Connector
50.8 mm
PDMS wall
1.5 cm
0.65 mm
3 mm
25.4 mm
Electrode 2
Counter / Reference
Working
Electrode 1
Galvanostat
Top View (b)

Figure 3

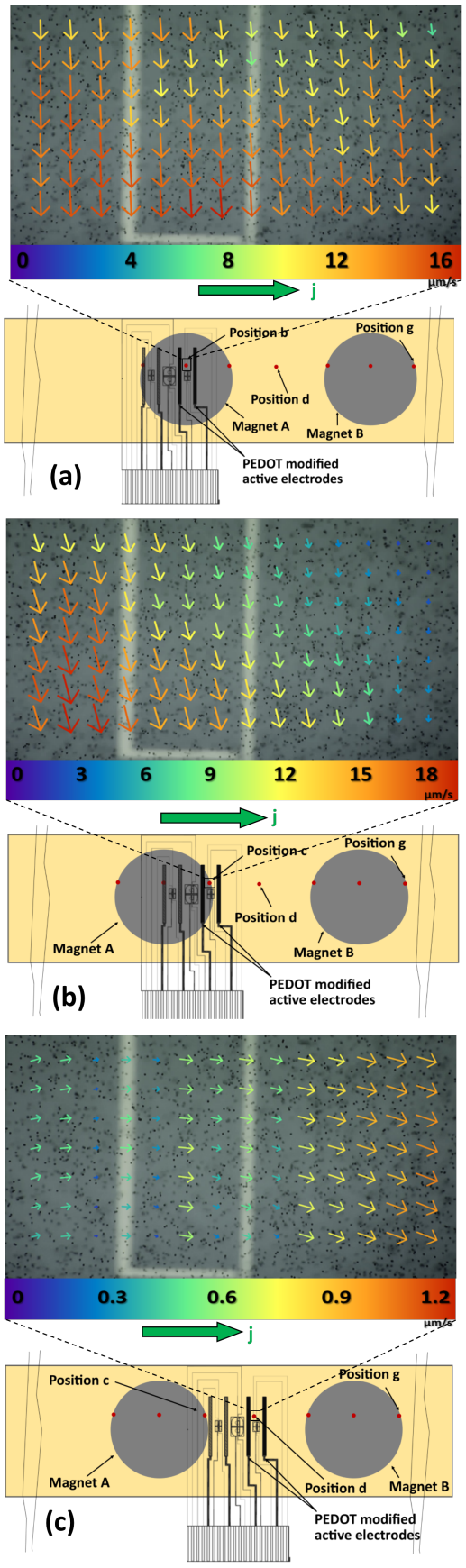
0
4
8
12
16
µm/s
j
Position b
Position g
Position d
Magnet A
Magnet B
PEDOT modified
active electrodes
(a)
0
3
6
9
12
15
18
µm/s
j
Position c
Position g
Position d
Magnet A
Magnet B
PEDOT modified
active electrodes
(b)
0
0.3
0.6
0.9
1.2
µm/s
j
Position c
Position g
Magnet A
Position d
Magnet B
PEDOT modified
active electrodes
(c)

Figure 4

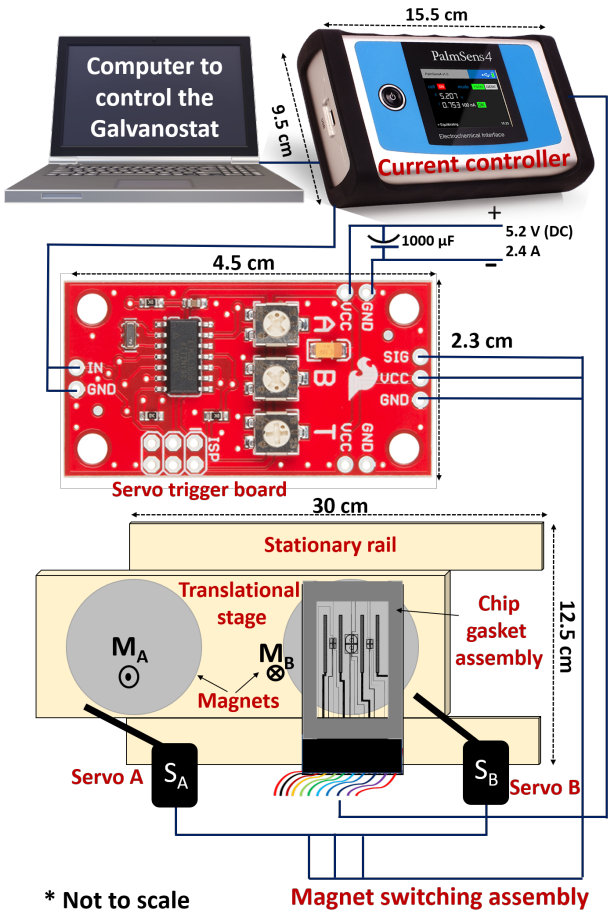
15.5 cm
Computer to control the Galvanostat
9.5 cm
PalmSens4
Current controller
+
5.2 V (DC)
2.4 A
1000 µF
−
4.5 cm
2.3 cm
IN
GND
SIG
VCC
GND
Servo trigger board
30 cm
Stationary rail
Translational stage
Chip gasket assembly
12.5 cm
M_A
M_B
Magnets
Servo A
S_A
S_B
Servo B
* Not to scale
Magnet switching assembly

Figure 5

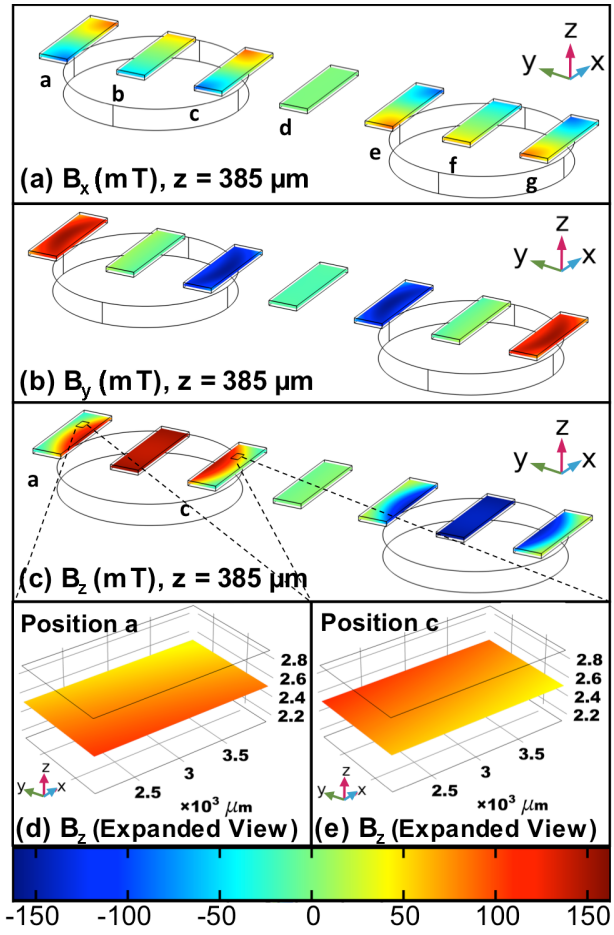
a
b
c
d
e
f
g
z
y
x
(a) B_x (m T), z = 385 µm
(b) B_y (m T), z = 385 µm
(c) B_z (m T), z = 385 µm
Position a
Position c
2.8
2.6
2.4
2.2
3.5
3
2.5
×10³ µm
(d) B_z (Expanded View)
(e) B_z (Expanded View)
-150
-100
-50
0
50
100
150

Figure 6

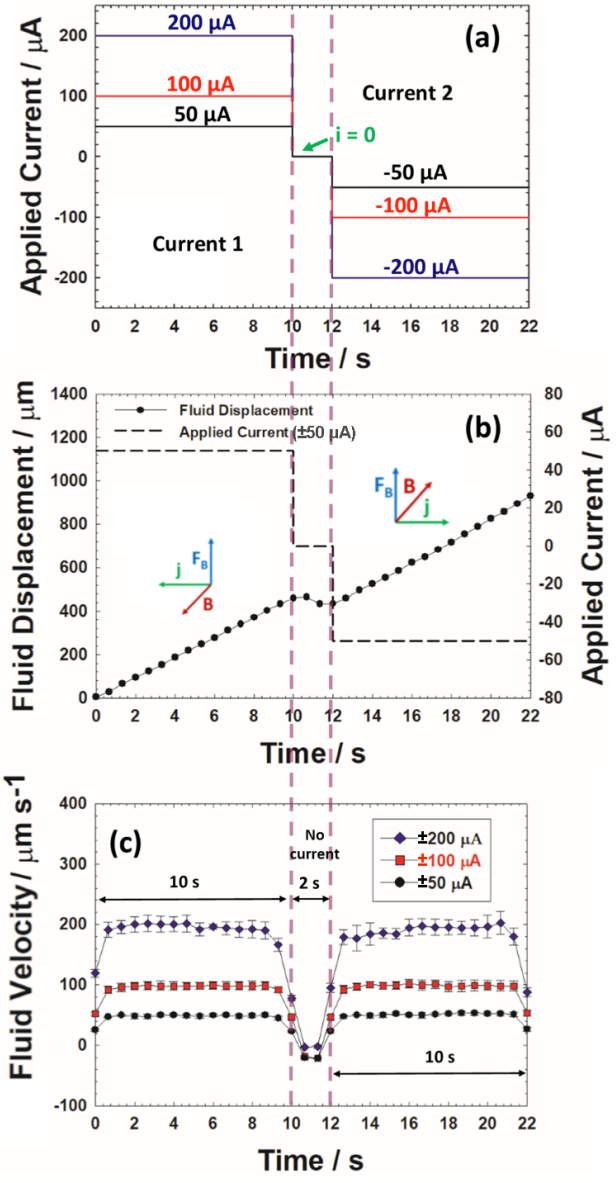
(a)
200 µA
100 µA
50 µA
Current 2
i = 0
-50 µA
-100 µA
-200 µA
Current 1
Applied Current / µA
Time / s
(b)
Fluid Displacement
Applied Current (±50 µA)
F_B
B
j
Fluid Displacement / µm
Applied Current / µA
Time / s
(c)
No current
10 s
2 s
±200 µA
±100 µA
±50 µA
10 s
Fluid Velocity / µm s-1
Time / s

Supporting Information

Sustaining Redox-Magnetohydrodynamics (R-MHD) Microfluidics by Switching Permanent Magnets: Synchronized Activation and Automation

Foysal Z. Khan (mzkhan@uark.edu), Department of Chemistry and Biochemistry, University of Arkansas, Fayetteville

Miguel Abrego Tello (maabrego@uark.edu), Department of Chemistry and Biochemistry, University of Arkansas, Fayetteville

David N. Parette (dparette@uark.edu), Department of Chemistry and Biochemistry, University of Arkansas, Fayetteville

Ingrid Fritsch* (ifritsch@uark.edu), Department of Chemistry and Biochemistry, University of Arkansas, Fayetteville

Supporting Information

Supporting information includes details of electrode fabrication and numerical approximations; photographs of a chip before and after PEDOT deposition on electrodes; CV responses during electrodeposition of PEDOT; CV, CP, and CA characterization of PEDOT films in aqueous electrolyte; details of manual and automated magnet switching apparatuses; PIV analysis of horizontal flow profiles; various graphical representations of numerical approximations (from COMSOL Multiphysics) of magnetic flux densities across the manual magnet switching assembly; a comparison of measured and simulated magnetic flux densities at magnet surfaces; and a video of automated magnet switching and resulting R-MHD fluid flow.

Details of Microelectrode Fabrication

The electrodes on the microfluidic chip were prepared by conventional photolithography processes, which generally follow earlier work from our laboratory.[8, 16] Here, we only briefly describe the microelectrode fabrication process. Silicon (100) wafers, purchased from Silicon Quest International, Santa Clara, CA (125 mm diameter, 600-650 μm thickness, with a 2-μm oxide layer) were used as the substrate material for the chips. The primary cleaning process for the wafers that was used is often termed as "RCA-1 clean". This involves preparing a solution of deionized (DI) water, ammonium hydroxide (30%), and hydrogen peroxide (30%) at a 5:1:1 (v/v/v) ratio, and then immersing the wafers secured in a Teflon career in the solution for 10 min with constant stirring at 75^{o} C. After removing the Teflon career from solution bath, the wafers were rinsed by spraying with DI water. After spray rinsing, the Teflon career with wafers was placed in a "Spin Rinse Dryer (SRD)" for final rinsing with DI water again and drying. Then, a ~10 nm chromium adhesion layer and a ~250 nm gold layer were deposited sequentially on the wafer by thermal vapor deposition.

One photoplot mask was designed for the gold microelectrode pattern and another one for the insulator layer (BCB, benzo cyclobutene) using AutoCAD. The photoplots were achieved from Fineline Imaging Inc, Colorado Springs, CO. The microelectrode pattern from the mask was transferred by photolithography to a layer of positive photoresist (AZ 4330) that was spin-coated onto the wafer. After developing with tetramethylammonium hydroxide solution, exposed metals were removed by gold and chromium etchant, creating the gold electrode-lead-contact pad pattern, and the remaining photoresist was removed. In the next step, a ~5 μm BCB layer was spin-coated onto the gold-patterned wafer which was then exposed to UV light through insulator layer mask,

developed, and cured. This latter step left the band electrodes and contact pads exposed. Each wafer (consisting of six chips) was then diced into individual chips.

Numerical Approximations of Magnetic Flux Density using COMSOL Multiphysics®

COMSOL Multiphysics®, a simulation environment that encompasses all the steps in the modeling workflow from defining geometries, material properties, and physics describing specific phenomena, models real-world applications by implementing numerical approximations. The analyses of magnetic flux density were performed with COMSOL Multiphysics® platform, version 5.5 coupled with the AC/DC Module add-on. These studies were computed with an Intel Core i7 8700K (processor), ASRock Z390 Pro4 (Motherboard) with Corsair DDR4-2400 128 GB (4x32 GB) of memory. The number of degrees of freedom solved was 70,359,736. A 3D model using the AC/DC Module Physics interface, employing Maxwell's equations was used to describe the electromagnetic field, forming the basis of classical electrodynamics. This set of four differential equations describe how electric and magnetic fields propagate, interact, or are influenced by objects by representing Coulomb's law, Faraday's laws of electromagnetic induction, the absence of magnetic monopoles, and a generalization of Ampère's law. They are solved using the finite element method with numerically stable edge element discretization. More specifically, this model uses the Magnetic Fields, No Currents interface, which characterizes the magnetostatics in current free regions by solving the magnetic flux conservation equation for the magnetic scalar potential (V_m), thus stating the relationships between the fundamental electromagnetic quantities. The physics interface solves Gauss' Law for the magnetic field using

the scalar magnetic potential as the dependent variable (V_m). This is explained in the AC/DC Module User's Guide.[3]

The main node, Magnetic Flux Conservation, relates the forces with which the magnets act on the surrounding medium (air), providing an interface for defining the constitutive relation and the relevant material properties, such as the relative permeability. The permeability of free space in a vacuum ($\mu_0=4\pi10^{-7}$) is a proportionality constant that exists between the magnetic flux density and magnetic field strength. The relative permeability is the ratio of the permeability of a specific medium to the permeability of free space (μ_0). The relative permeability indicates how easily a material can become polarized by the imposition of an electric field on an insulator. The air relative permeability is 1.00. The two magnets show a characteristic remanent flux density of ±1.2 T in the z-component for magnets A and B, respectively. The dimensions and placement of the two cylindrical magnets in the manual magnet assembly are the same as used in the numerical simulations: 12.7 mm radius and 3.175 mm height, with a distance between the innermost edges of the magnets A and B of 25 mm.

The mesh resolution and mesh quality element are crucial aspects that were considered when validating the model. Low mesh resolution and mesh quality element lead to inaccurate results. The mesh resolution is dependent upon the system considerations. The mesh quality is dependent upon the irregularities of the shapes of the mesh elements and defined as a dimensionless quantity between 0 and 1. A mesh quality of 1 would represent a perfectly regular element, and a mesh quality of 0 represents a degenerated element. The skewness (the default quality measure in COMSOL Multiphysics®) of the model shows a minimum element quality of 0.1843 and an average element quality of 0.6633. The mesh for this model consists of the User-Controlled mesh. The User-Controlled mesh generated the mesh directly using subnodes to this mesh consisting of

free tetrahedral sequences. The free tetrahedral sequences were calibrated for general physics. The mesh customization required three spheres of different radii representing the system domain (environment), two cylinders representing magnets A and B and seven boxes at the viewing regions. The innermost sphere has a maximum element size of 500 μm, minimum element size of 35 μm, maximum element growth rate of 1.3, curvature factor 0.2 and resolution of narrow regions of 1. The middle sphere has a maximum element size of 1500 μm, minimum element size of 100 μm, maximum element growth rate of 1.3, curvature factor 0.2 and resolution of narrow regions of 1. The outer sphere has a maximum element size of 3900 μm, minimum element size of 150 μm, maximum element growth rate of 1.3, curvature factor 0.2 and a resolution of narrow regions of 1. The outer sphere has an infinite element domain node that applies a real-valued coordinate scaling to a layer of virtual domain in the physics of interest. The analysis of residuals plays an important role in validating the regression model. The magnetic flux density residuals in x, y, and z are in order of 10^{-10}.

References

[1] M.C. Weston, M.D. Gerner, I. Fritsch, Magnetic Fields for Fluid Motion, Anal Chem, 82(2010) 3411-8.
[2] J. Rumble, CRC Handbook of Chemistry and Physics, 100th ed.: CRC Press; 2020.
[3] L. Wang, L. Flanagan, A.P. Lee, Side-Wall Vertical Electrodes for Lateral Field Microfluidic Applications, J Microelectromech Sys, 16(2007) 454-61.
[4] A. Homsy, V. Linder, F. Lucklum, N.F. de Rooij, Magnetohydrodynamic pumping in nuclear magnetic resonance environments, Sens Actuat B-Chem, 123(2007) 636-46.
[5] A. Homsy, S. Koster, J.C.T. Eijkel, A. van den Berg, F. Lucklum, E. Verpoorte, et al., A high current density DC magnetohydrodynamic (MHD) micropump, Lab Chip, 5(2005) 466-71.
[6] P.U. Arumugam, E.S. Fakunle, E.C. Anderson, S.R. Evans, K.G. King, Z.P. Aguilar, et al., Redox Magnetohydrodynamics in a Microfluidic Channel: Characterization and Pumping, J Electrochem Soc, (2006) E185-E94.
[7] M.C. Weston, I. Fritsch, Manipulating Fluid Flow on a Chip Through Controlled-Current Redox Magnetohydrodynamics, Sens Actuat B-Chem, 173(2012) 933-44.
[8] V. Sahore, I. Fritsch, Flat Flow Profiles Achieved with Microfluidics Generated by Redox-Magnetohydrodynamics, Anal Chem, 85(2013) 11809-16.

[9] F. Gao, A. Kreidermacher, I. Fritsch, C.D. Heyes, 3D Imaging of Flow Patterns in an Internally-Pumped Microfluidic Device: Redox Magnetohydrodynamics and Electrochemically-Generated Density Gradients, Anal Chem 85(2013) 4414−22.
[10] C. Das, G. Wang, F. Payne, Some practical applications of magnetohydrodynamic pumping, Sens Actuat A-Phys, 201(2013) 43-8.
[11] V. Sahore, I. Fritsch, Microfluidic rotational flow generated by redox-magnetohydrodynamics (MHD) under laminar conditions using concentric disk and ring microelectrodes, Microfluid Nanofluid, 18(2015) 159-66.
[12] V. Hähnel, F.Z. Khan, G. Mutschke, C. Cierpka, M. Uhlemann, I. Fritsch, Combining magnetic forces for contactless manipulation of fluids in microelectrode-microfluidic systems, Sci Rep, 9(2019) 5103.
[13] V. Sahore, I. Fritsch, Redox-Magnetohydrodynamics, Flat Flow Profile-Guided Enzyme Assay Detection: Toward Multiple, Parallel Analyses, Anal Chem, 86(2014) 9405-11.
[14] M.C. Weston, C.K. Nash, I. Fritsch, Redox-Magnetohydrodynamic Microfluidics Without Channels and Compatible with Electrochemical Detection Under Immunoassay Conditions, Anal Chem, 82(2010) 7068-72.
[15] S. Qian, H.H. Bau, Magneto-hydrodynamic stirrer for stationary and moving fluids, Sensor Actuat B-Chem, 106(2005) 859-70.
[16] E.C. Anderson, M.C. Weston, I. Fritsch, Investigations of Redox Magnetohydrodynamic Fluid Flow At Microelectrode Arrays Using Microbeads, Anal Chem, 82(2010) 2643-51.
[17] V. Sahore, A. Kreidermacher, F.Z. Khan, I. Fritsch, Visualization and Measurement of Natural Convection from Electrochemically-Generated Density Gradients at Concentric Microdisk and Ring Electrodes in a Microfluidic System, J Electrochem Soc, 163(2016) H3135-H44.
[18] K. Ngamchuea, S. Eloul, K. Tschulik, R.G. Compton, Advancing from rules of thumb: quantifying the effects of small density changes in mass transport to electrodes. Understanding natural convection, Anal Chem, (2015) DOI: 10.1021/acs.analchem.5b01293.
[19] A.V. Lemoff, A.P. Lee, An AC magnetohydrodynamic micropump, Sens Actuat B-Chem, 63(2000) 178-85.
[20] A.V. Lemoff, A.P. Lee, An AC Magnetohydrodynamic Microfluidic Switch for Micro Total Analysis Systems, Biomed Microdevices, 5(2003) 55-60.
[21] J. West, B. Karamata, B. Lillis, J.P. Gleeson, J. Alderman, J.K. Collins, et al., Application of magnetohydrodynamic actuation to continuous flow chemistry, Lab Chip, 2(2002) 224-30.
[22] J.C.T. Eijkel, C. Dalton, C.J. Hayden, J.P.H. Burt, A. Manz, A circular ac magnetohydrodynamic micropump for chromatographic applications, Sens Actuat B-Chem, 92(2003) 215-21.
[23] C.K. Nash, The 2014 Colin G. Fink Summer Research Fellowship — Summary Report: Advanced Microfluidic Pumping at Poly(3,4-ethylenedioxythiophene)-Modified Electrodes via AC-Magnetohydrodynamics, The Electrochemical Society Interface, 23(2014) 79-80.
[24] C.K. Nash, I. Fritsch, Poly(3,4-ethylenedioxythiophene)-Modified Electrodes for Microfluidics Pumping with Redox-Magnetohydrodynamics: Improving Compatibility for Broader Applications by Eliminating Addition of Redox Species to Solution, Anal Chem, 88(2016) 1601-9.
[25] F.Z. Khan, I. Fritsch, Chip-Scale Electrodeposition and Analysis of Poly(3,4-ethylenedioxythiophene) (PEDOT) Films for Enhanced and Sustained Microfluidics Using DC-Redox-Magnetohydrodynamics, J Electrochem Soc, 166(2019) H615-H27.
[26] F.Z. Khan, J.A. Hutcheson, C.J. Hunter, A.J. Powless, D. Benson, I. Fritsch, et al., Redox-Magnetohydrodynamically Controlled Fluid Flow with Poly(3,4-ethylenedioxythiophene) Coupled to an Epitaxial Light Sheet Confocal Microscope for Image Cytometry Applications, Anal Chem, 90(2018) 7862-70.
[27] D. Brown, Tracker: Video Analysis and Modeling Tool, 2020.
[28] I. Fritsch, F.Z. Khan, D. Parette, Magnetohydrodynamic Microfluidic Systems Including Modified Electrodes And Methods Of Using The Same, BOARD OF TRUSTEES OF THE UNIVERSITY OF ARKANSAS (Little Rock, AR, US), US, 2020.

Video

Video S-1. Operation of the automated magnet switching assembly that is synchronized to swap 0.37 T magnets of opposite field orientation when electrodes are brought momentarily to open circuit, after which a current of an opposite bias was applied. To perform R-MHD pumping, the PEDOT-modified band electrodes (1.5 cm long, 650 μm wide, and with 3 mm gap between them) are positioned over the center of the magnet for 10 s while a current is applied (here it is +50 μA or -50μA). The electrodes change to open circuit for 2 s and the magnet assembly, triggered by the galvanostat through a controller board, switches the magnets beneath the R-MHD chamber. The corresponding R-MHD fluid flow is also visualized here by monitoring microbead movement in a "buffer / glycerol / bead" solution, focused on a horizontal plane at 640 μm above the floor of the 762-μm high chamber. The solution comprised of an aliquot of 400 μL PBS: glycerol electrolyte (v/v, 70% 0.01 M PBS with 30% proteome grade glycerol) and 12 μL of 10 μm polystyrene beads. The "0.01 M PBS" consisted of 0.01 M phosphate, 0.0027 M potassium chloride, and 0.137 M sodium chloride, pH 7.4 at 25°C.

Table

Table S-1. Comparison of experimental measurements and numerical approximations of magnetic flux densities across the manual magnet assembly. Positions are as indicated in Figures 5 and 6 in the main document. Positions a, b, and c reside over Magnet A. Positions e, f, and g reside over Magnet B. Magnetometer sensor dimensions are 1450 μm× 1450 μm×600 μm. Numerical approximation values consider volume occupied by sensor. Seven xy planes were measured at different probe thicknesses (z = 0 μm, 100 μm, 200 μm, 300 μm, 400 μm, 500 μm, and 600 μm). Three lines including entire sensor width (1450 μm) were averaged across three length sensor positions (x=0 μm, 725 μm, 1450 μm) for each position of chip over magnet assembly. Unlike experimental magnets, simulated magnets have sharp edges, which results in a higher percent difference at the edges.

	Experiments		**COMSOL Multiphysics**								**% Difference in B_z between Numerical Approximations and Experimental Values**
	Average of Measurements (N = 5)		**Average of Numerical Approximations (N=189)**								
Position of Chip Over Magnet Assembly	**Bz (mT)**		**Bx (mT)**		**By (mT)**		**Bz (mT)**		**|B| (mT)**		
a	207.5	(±3.2)	7.21	(±0.31)	139	(±5)	257	(±18)	293	(±13)	24%
b	141.2	(±2.4)	1.32	(±0.13)	0	(±0)	146	(±1)	146	(±1)	3%
c	238.9	(±4.8)	7.12	(±0.24)	-139	(±5)	257	(±18)	294	(±13)	8%
e	-222.2	(±1.3)	7.05	(±0.20)	-139	(±5)	-259	(±18)	295	(±13)	17%
f	-151.6	(±0.5)	1.32	(±0.13)	0	(±0)	-146	(±1)	146	(±1)	-4%
g	-232.1	(±2.0)	7.10	(±0.26)	139	(±5)	-257	(±18)	293	(±13)	11%

Figures

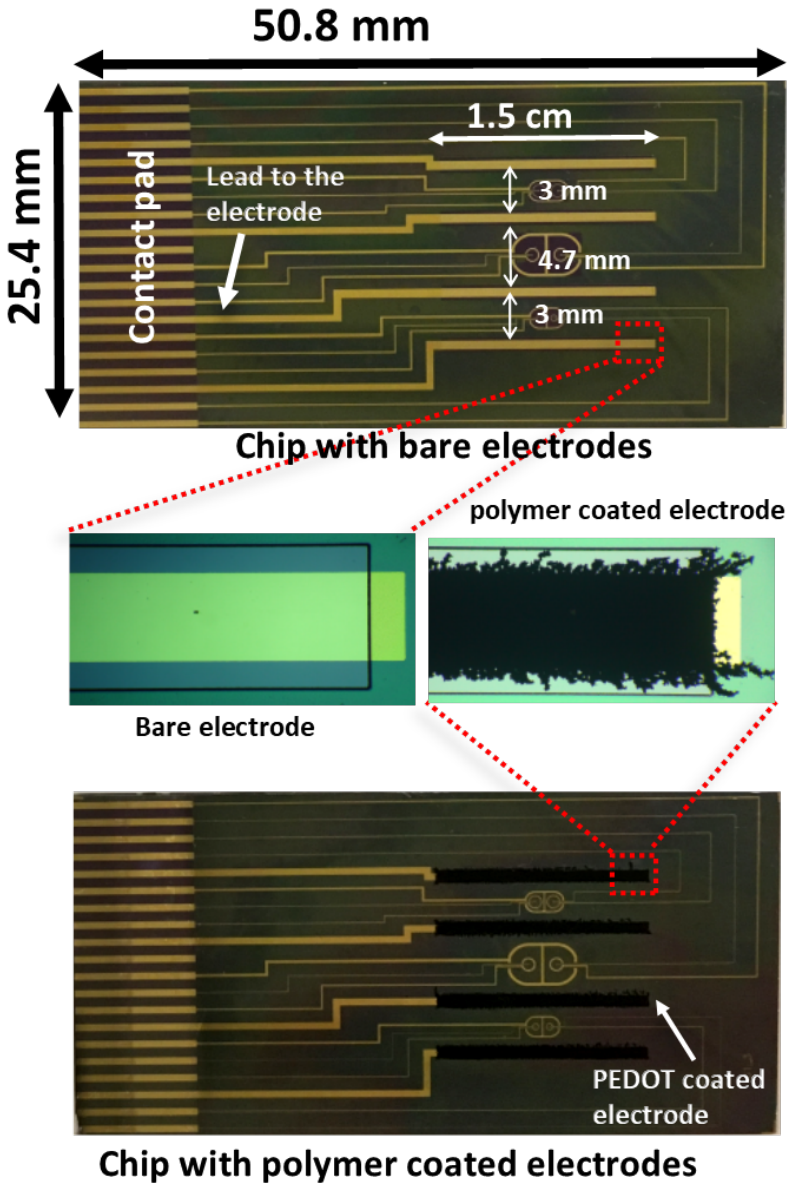

Figure S-1: (Top figure) Photograph of electrode chip before electrodeposition of PEDOT. Each chip has dimensions of 50.8 × 25.4 mm (1 in. × 2 in.) and four individually addressable band electrodes. Other electrodes are also available but were not used in the studies reported herein. The active region (exposed to solution) of each gold band electrode is 1.5 cm long and 650 µm wide. The two outermost electrode pairs are separated by 3 mm whereas the middle two electrodes are separated by 4.7 mm. Each electrode may be electronically connected with the current controller (the PalmSens4) through contact pads and an edge connector (not shown here). (Middle figures) Expanded pictures showing the end of a single bare gold and PEDOT-coated band electrode. The black outline defines the edge of the insulating benzocyclobutene layer. (Bottom figure) Photograph of entire chip after electrodeposition of PEDOT films on all the four band electrodes.

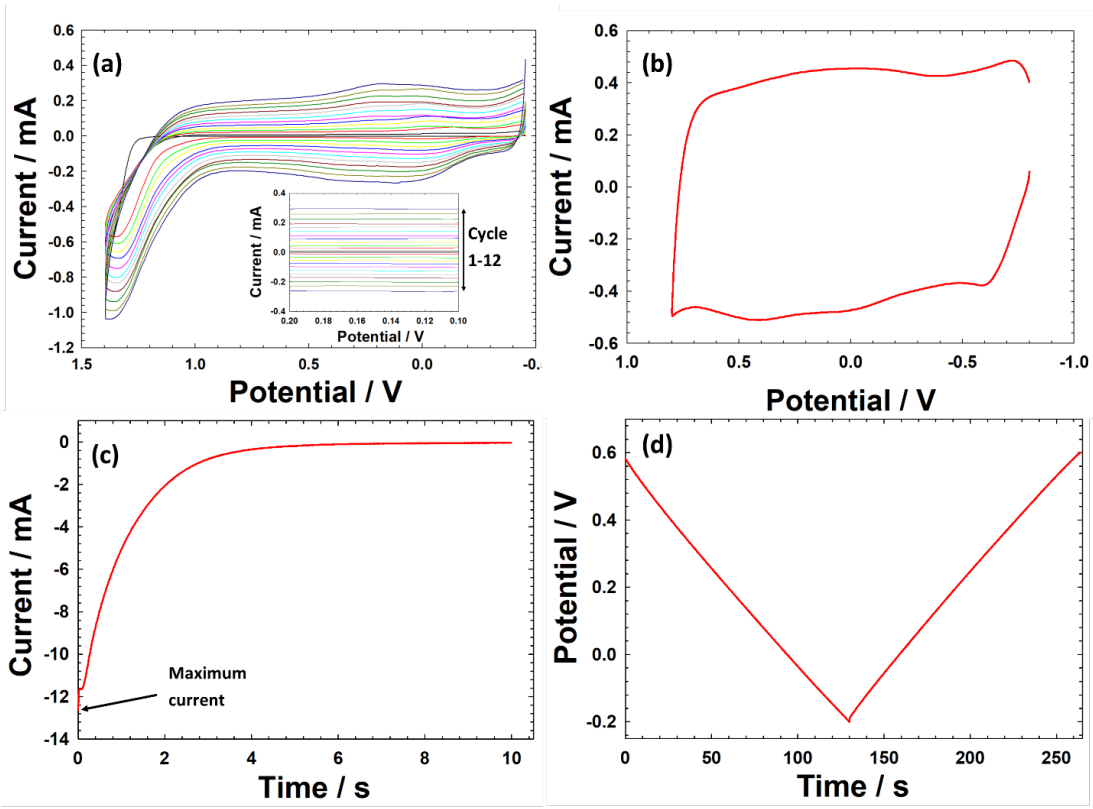

Figure S-2: (a) CV responses during electropolymerization of a single band electrode in propylene carbonate solution containing 0.010 M EDOT and 0.100 M $TBAPF_6$ over a potential window of -0.455 to 1.40 V for 12 sequential CV cycles at 5 mV/s. (b) CV characterization of PEDOT modified electrode at 50 mV/s in PBS: glycerol (v/v, 70% 0.01 M PBS with 30% proteome grade glycerol) solution. (c) A representative CA response acquired by holding the potential at -0.80 V for 10 s and then stepping to +0.80 V for 10 s. (d) A representative CP response acquired by applying ±50 µA current with potential cutoffs of -0.20 and 0.60 V. For all experiments here, a three-electrode cell was used with a Ag/AgCl (saturated KCl) reference and Pt flag counter electrodes with 20 mL of monomer solution or characterizing solution in a 20 mL glass beaker. In these figures, the sign convention for cathodic current is positive.

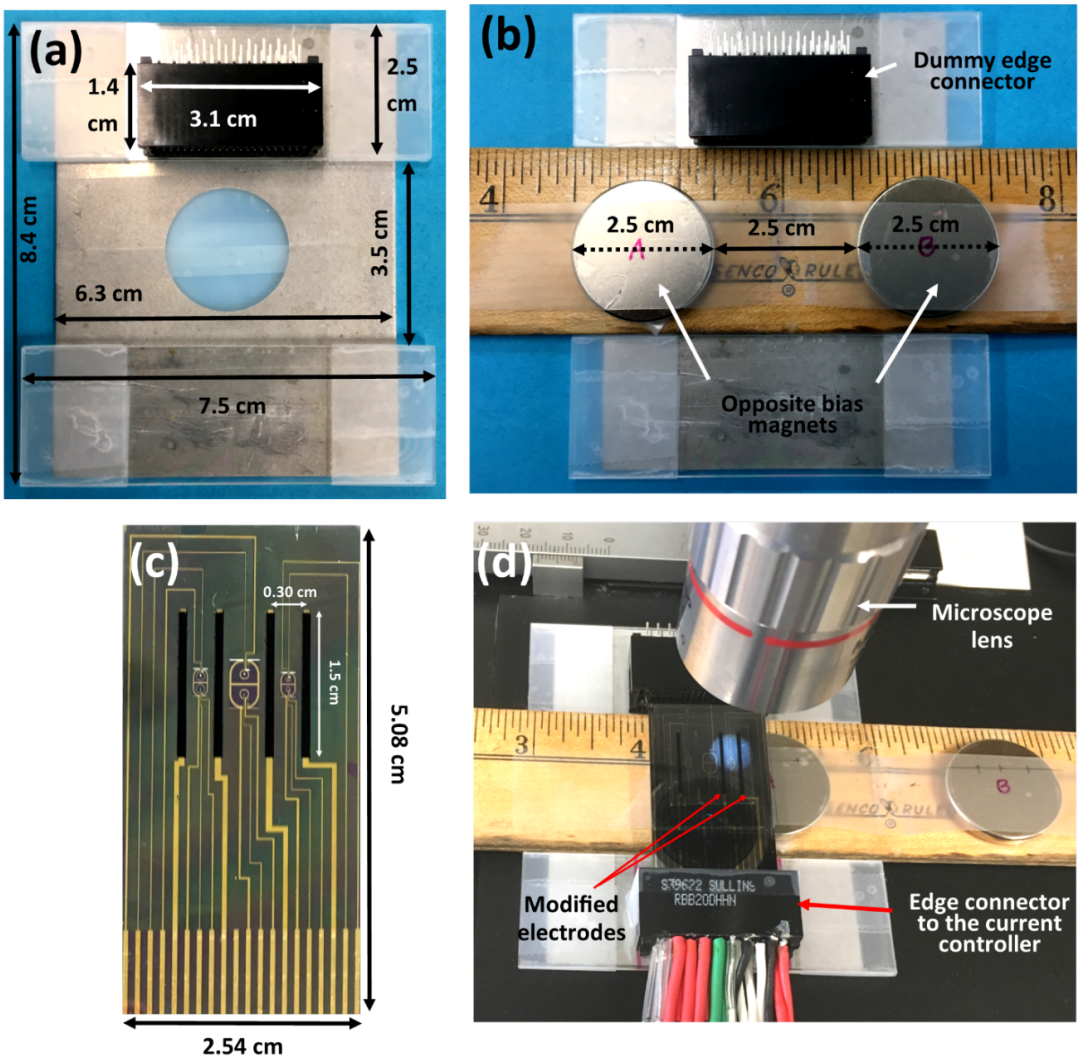

Figure S-3: Details of manual magnet switching apparatus. (a) Chip-magnet holder assembly where the base is made of stainless-steel block (8.4 × 6.3 × 0.15 cm) and two sets of glass slides (7.5 × 2.5 × 0.20 cm) were taped on the top and bottom portion of the stainless-steel block. An edge connector is taped on the top set of slides into which the non-contact end of the chip is inserted to hold the chip still and level. (b) Two magnets of opposite field orientations (each ~ 0.14 T, 3.5 cm diameter and 1.27 cm height, grade N40 and separated by 2.5 cm were taped on a wooden ruler (3.3 cm wide and 0.20 cm thick) that could move back and forth in the gap between the two sets of glass slides. (c) Chip with PEDOT-coated band electrodes. (d) Complete assembly on microscope stage where the R-MHD microfluidic chamber (chip (with PEDOT coated electrodes), gasket and coverslip) is placed on top to fit perfectly level on the stage and so that the wooden ruler with magnets moves freely beneath it, leaving a 1.5-mm gap between the bottom surface of the chip and the top surfaces of the magnets.

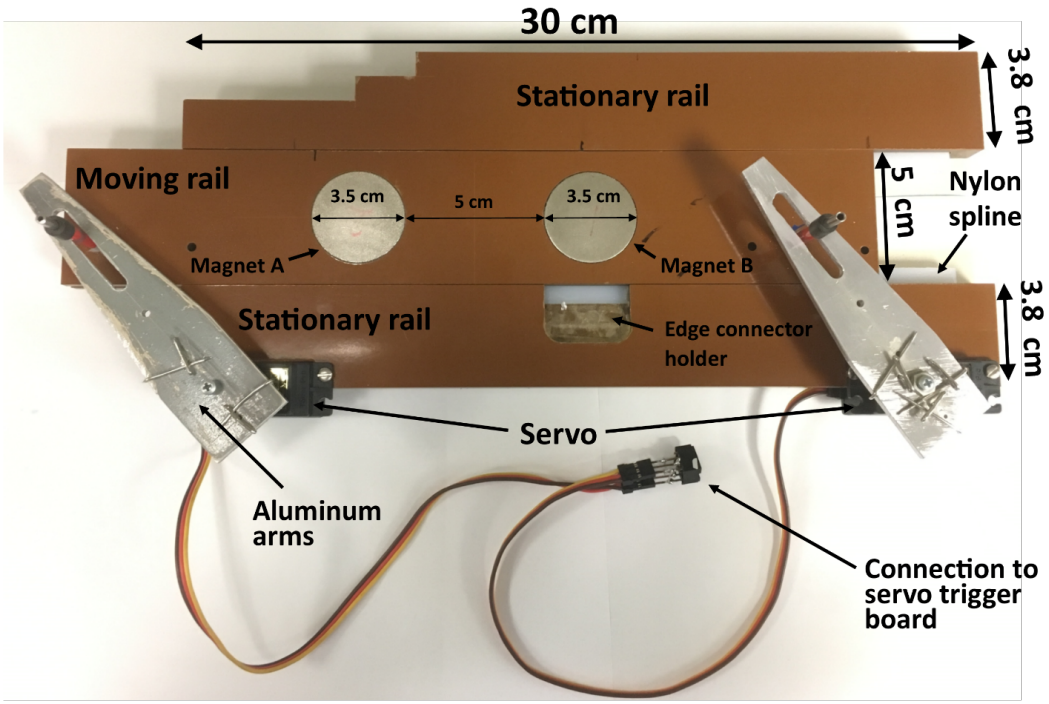

Figure S-4: The top-down view of the servo-driven (automated) magnet switching assembly. The moving rail slides between two stationary rails. Two permanent magnets with oppositely oriented fields were press-fit into the bored holes on the moving rail. Two standard servos were fixed to two sites on the bottom stationary rail and each one was attached to machine-milled aluminum arms that allow conversion of rotational motion of the servos to linear motion in the moving rail.

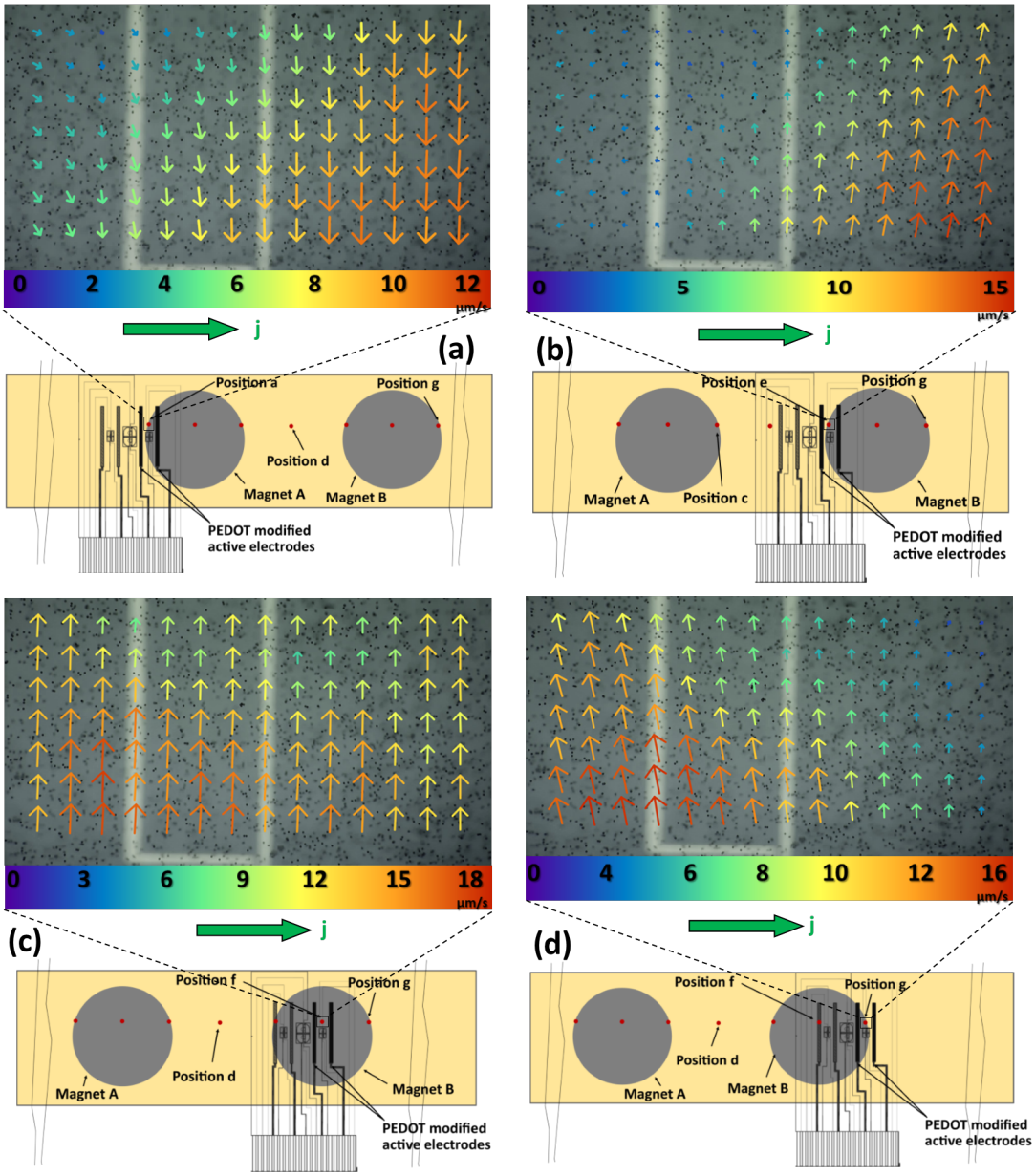

Figure S-5: Top-down views of the chip placement over the manual magnet switching assembly with dimensions shown in Figure S-3 at (a) position a, (b) position e, (c) position f, and (d) position g. The expanded views of (a)-(d) show the horizontal flow vectors as determined by PIV analysis of microbead motion at 385 µm above the floor of the microfluidic chamber at those positions over the magnet assembly. Evaluations were obtained at a total of seven different positions, three of which (positions b, c, and d) are shown in Figure 5 of the main document of the manuscript. A 50 µA cathodic current at Electrode 1 vs. Electrode 2 was maintained across the entire magnet assembly.

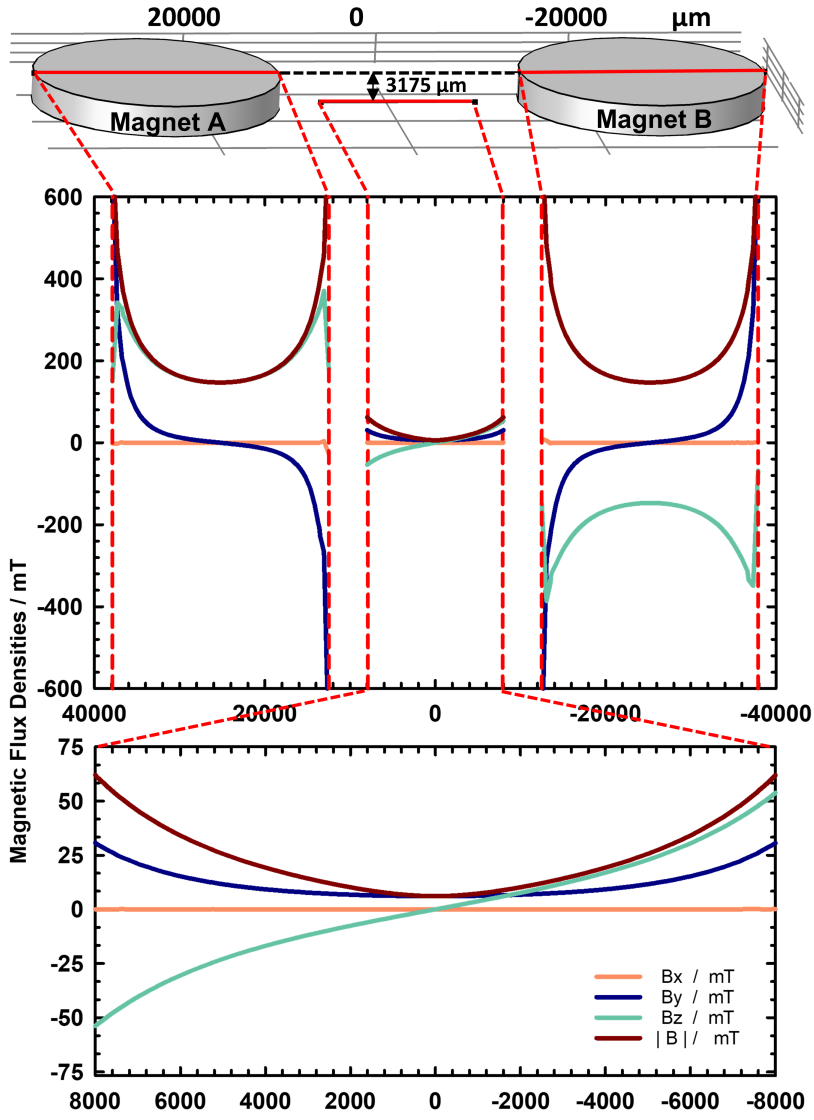

Figure S-6: Numerical approximations of magnetic flux densities across the manual magnet assembly in locations similar to where measurements were made with a magnetometer. For validation, the simulated results are compared to the experimental data obtained with a magnetometer in Table S-1. The measurements were taken along a horizontal line (in the y-direction) connecting the magnet centers. In the z-coordinate, over Magnets A and B, the magnetic flux densities are shown at the top surfaces. Between the magnets, the magnetic flux densities are shown at the ruler surface, 3175 µm below the top surfaces of the magnets, which is equal to the magnet thickness). The two magnets have opposite field orientations. The abscissa is in units of micrometers.

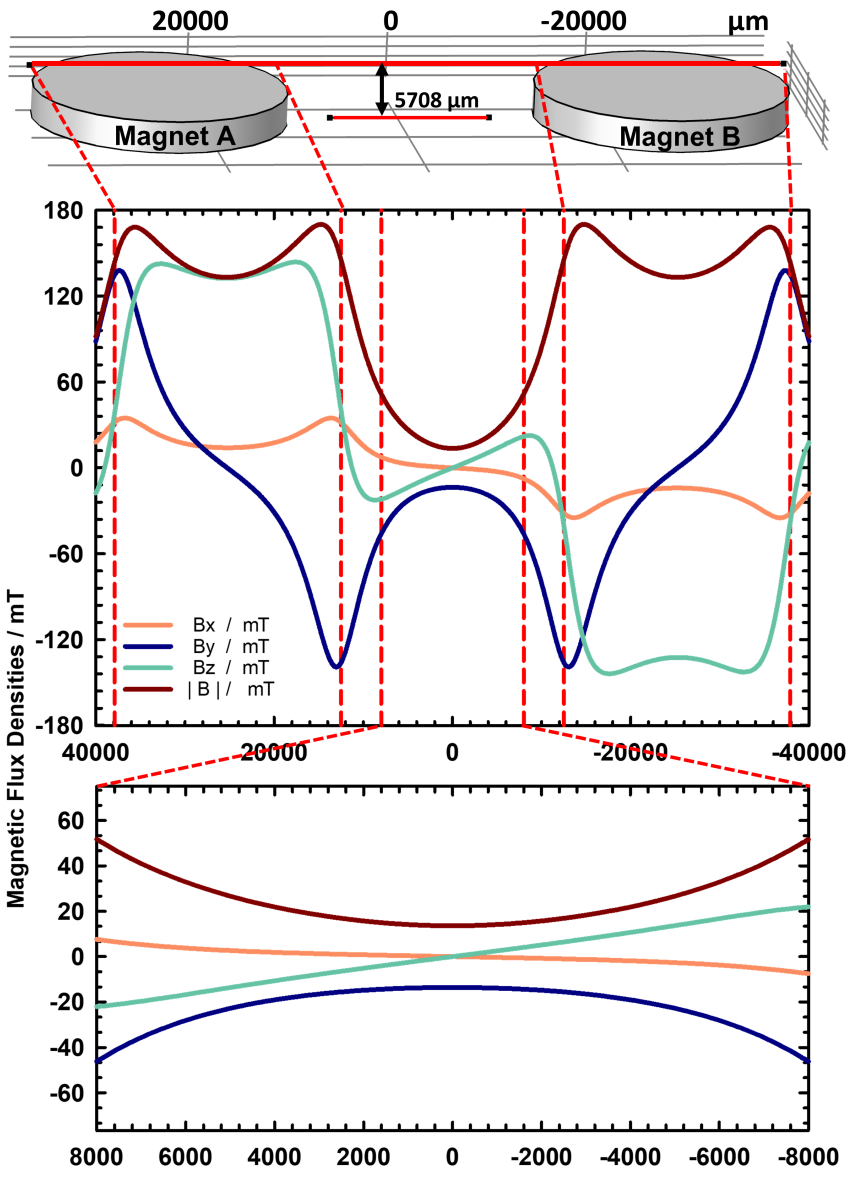

Figure S-7: Numerical approximations of magnetic flux densities across the manual magnet assembly in locations of the recorded videos in the MHD chamber as it passes across the assembly during a magnet-switching experiment. The measurements were taken along a horizontal line (in the y-direction) that is offset by 3000 µm (in the +x-direction) from a line connecting the magnet centers and 2533 µm (in the z direction) above the surfaces of the magnets and 5708 µm above the ruler, consistent with a location of 385 µm above the floor of the MHD chamber as the magnet assembly slides beneath the R-MHD apparatus. The two magnets have opposite field orientations. The abscissa is in units of micrometers.

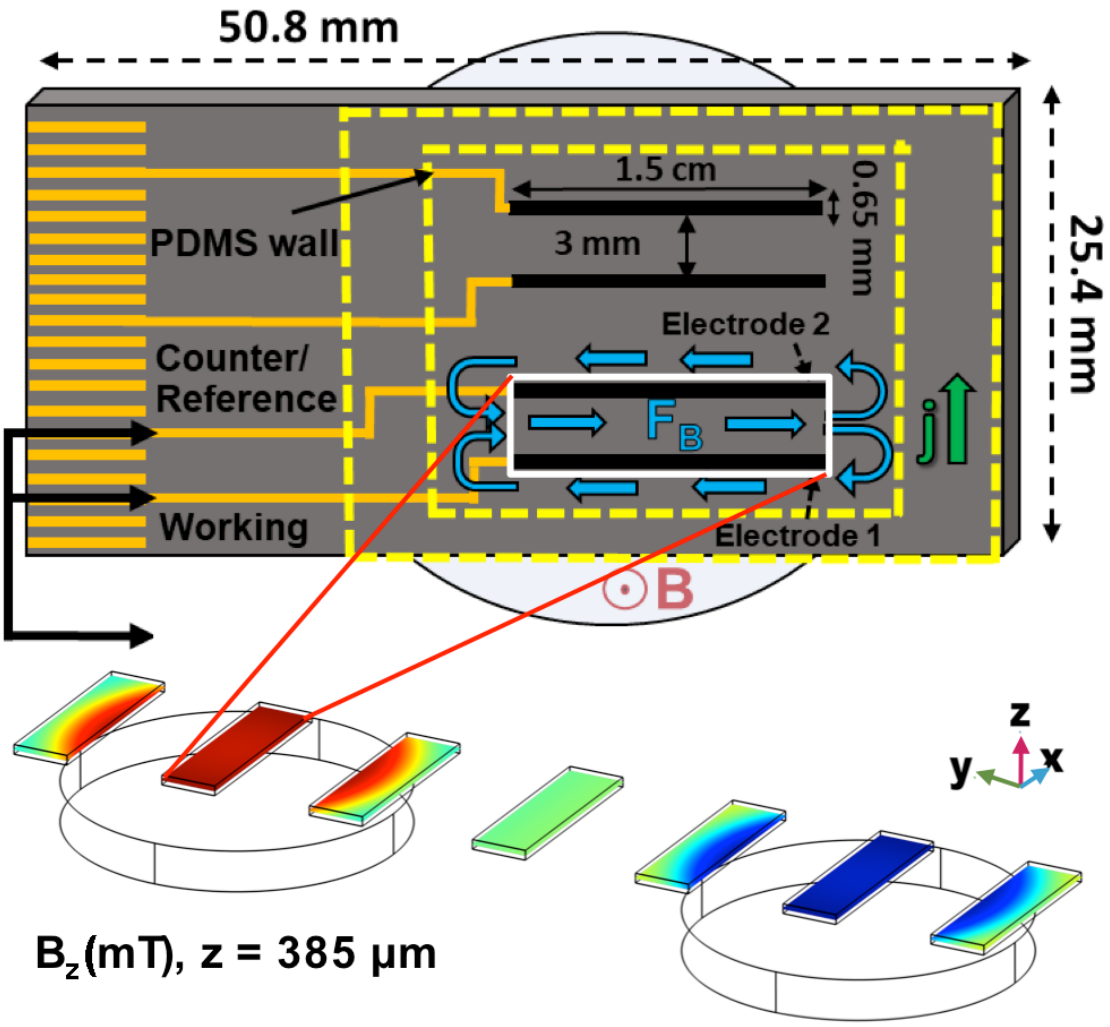

Figure S-8. Schematic showing the pumping region of the chip (a volume defined by the distance between outer edges of the pumping electrodes and their length, and the height of the PDMS gasket) where high-spatial resolution mapping of magnetic flux densities were determined by numerical approximations at different positions a, b, c, d, e, f, and g (from left to right) over the manual magnet assembly. The small black-outlined rectangles shown here only at positions a and c for clarity represent the video recording region used for PIV analysis. Figure 6 in the main document and Figures S-9 and S-10 in the Supporting Information follow this same layout. Here, B_z is shown at a height of 385 µm above the floor of the chamber at the seven different positions, and is the same as in Figure 6 in the main document.

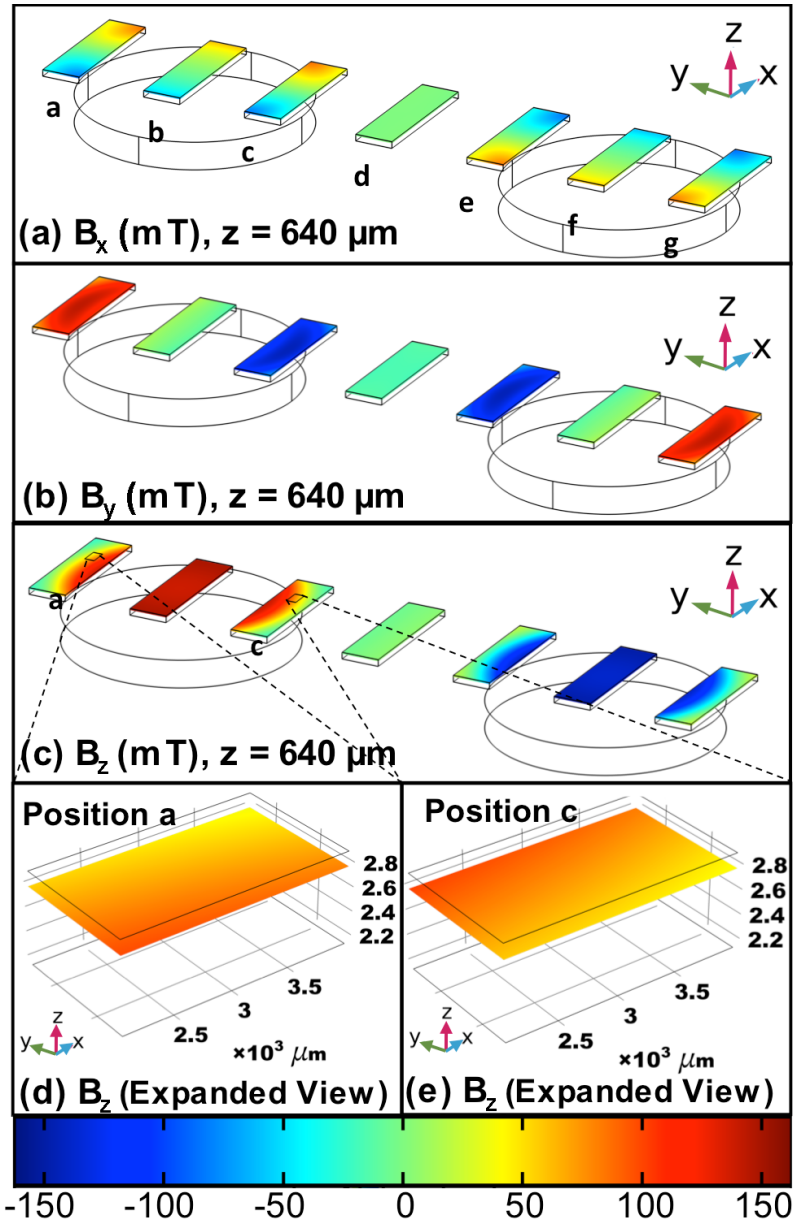

Figure S-9: Results using COMSOL Multiphysics® numerical approximation of the three components of magnetic flux density: (a) Bx, (b) By, and (c) Bz. Sections (d) and (e) consist of expanded views of B_z in the positions where PIV analyses of microbead motion were measured. Horizontal slices (xy planes) are shown through the space between outer edges of the activated band electrodes (4300 µm), along their length (1.5 cm) and at 640 µm from the floor of the chamber at seven different regions across the manual magnet assembly having dimensions as those shown in Figure S-3 of Supporting Information.

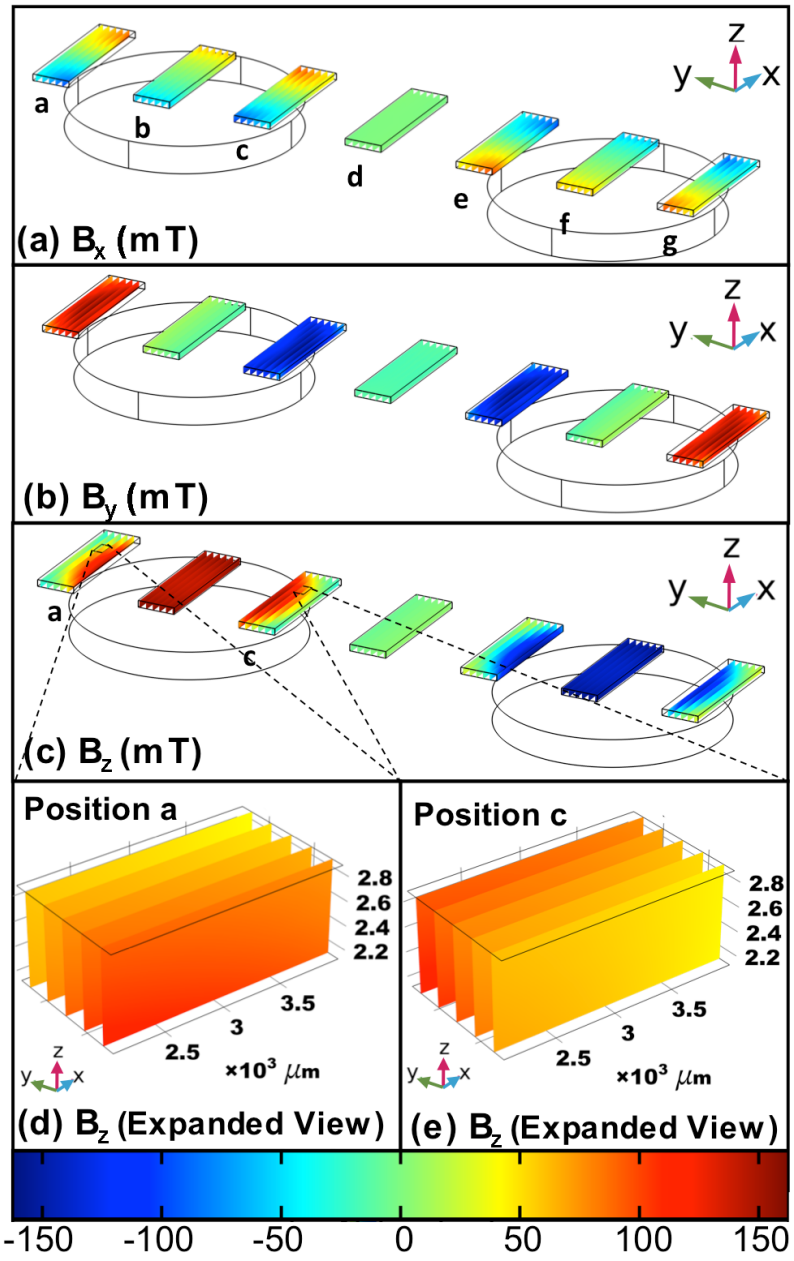

Figure S-10: Results using COMSOL Multiphysics® numerical approximation of the three components of magnetic flux density: (a) B_x, (b) B_y, and (c) B_z. Sections (d) and (e) consist of expanded views of B_z in the positions where PIV analyses of microbead motion were measured. Five to six vertical slices in xz plane, spaced 744 μm apart, are shown through the space between outer edges of the activated band electrodes (4300 μm), along their length (1.5 cm), and between the floor of the chamber to the lid (672 μm) at seven different locations across the manual magnet assembly having dimensions as those described in Figure S-3.